Astronomy & Astrophysics manuscript no. output
May 19, 2020

Type Ic supernovae from the (intermediate) Palomar Transient Factory

Barbarino, C. et al.[1]

The Oskar Klein Centre, Department of Astronomy, Stockholm University, AlbaNova, 10691 Stockholm, Sweden.
e-mail:

Received; accepted

ABSTRACT

Context. Type Ic supernovae represent the explosions of the most stripped massive stars, but their progenitors and explosion mechanisms remain unclear. Larger samples of observed supernovae can help characterize the population of these transients.
Aims. We present an analysis of 44 spectroscopically normal Type Ic supernovae, with focus on the light curves. The photometric data were obtained over 7 years with the Palomar Transient Factory (PTF) and its continuation, the intermediate Palomar Transient Factory (iPTF). This is the first homogeneous and large sample of SNe Ic from an untargeted survey, and we aim to estimate explosion parameters for the sample.
Methods. We present K-corrected *gri* light curves of these SNe, obtained through photometry on template-subtracted images. We performed an analysis on the shape of the *r*-band light curves and confirmed the correlation between the rise parameter Δm_{-10} and the decline parameter Δm_{15}. Peak *r*-band absolute magnitudes have an average of $-17-71 \pm 0.85$ mag. To derive the explosion epochs, we fit the *r*-band lightcurves to a template derived from a well sampled light curve. We computed the bolometric light curves using *r* and *g* band data, $g-r$ colors and bolometric corrections. Bolometric light curves and Fe II λ5169 velocities at peak were used to fit to the Arnett semianalytic model in order to estimate the ejecta mass M_{ej}, the explosion energy E_K and the mass of radioactive nickel $M(^{56}\mathrm{Ni})$ for each SN.
Results. Including all 41 SNe, we find average values of $< M_{ej} >= 4.39 \pm 0.31\ M_\odot$, $< E_K >= 1.71 \pm 0.16\ \times 10^{51}$ erg, and $< M_{^{56}\mathrm{Ni}} >= 0.19 \pm 0.05\ M_\odot$. The explosion parameter distributions are comparable to those available in the literature.

Key words. supernovae: general – supernovae: individual:

1. Introduction

Core-collapse supernovae (CC SNe) are the explosions of massive stars ($\gtrsim 8\ M_\odot$) which undergo gravitational collapse of the core at the end of their lifes. Their classification relies on the presence/absence of some spectroscopic features (e.g., Filippenko 1997). When they lack, partially or totally, hydrogen (H) or helium (He) they are called stripped envelope SNe (SE SNe). In this class we find SNe IIb, Ib and Ic. Type Ib SNe show no H but He in their spectra. SNe IIb show an initial signature of H at peak, which then disappears over time as their spectra become similar to those of Type Ib SNe. Supernovae Type Ic are the ones which lack both H and He. Two main scenarios have been proposed as progenitor systems of SE SNe: i) single and massive Wolf-Rayet (WR) stars that lose their outer envelopes through radiation-driven stellar winds (Begelman & Sarazin 1986; Woosley et al. 1995), and ii) lower mass stars in binary systems characterized by mass transfer (Wheeler & Levreault 1985; Podsiadlowski et al. 1992; Yoon et al. 2010). It is still a matter of debate whether one or both of these progenitor channels can explain the observed SE SN population. The estimated masses of the ejecta for SE SNe seem to favour the lower mass binary star scenario, rather than very massive single WR stars (Eldridge et al. 2013, Lyman et al. 2016, Cano et al. 2013); and for example the data for the individual Type Ib SN iPTF13bvn seem to be more consistent with a binary system (Bersten et al. 2014; Fremling et al. 2014, 2016; Eldridge et al. 2015). However, some SE SNe do seem to be originating from very massive stars (e.g. SN 2011bm, Valenti et al. 2012; OGLE-2014-SN-131, Karamehmetoglu et al. 2017; LSQ14efd, Barbarino et al. 2017) and thus favour a single progenitor system.
The photometric samples available in the literature either refer to SE SNe (Lyman et al. 2016; Prentice et al. 2016; Taddia et al. 2018b, Prentice et al. 2019) or to SNe Ibc (Drout et al. 2011; Taddia et al. 2015) including both SNe Ib and Ic. A major sample of only SNe Ic (or Ib) has not been available. Thanks to the untargeted surveys, the Palomar Transient Factory (PTF, Rau et al. 2009; Law et al. 2009) and its continuation, the intermediate Palomar Transient Factory (iPTF, Kulkarni 2013), we can here present optical observations of a large (44 objects) and homogeneous sample of spectroscopically normal SNe Ic. This enables a study of the properties of this SN population and their progenitor stars.
The paper is organized as follow: in Sect. 2 we present the sample while the photometry and the data reduction are presented in Sect. 3. The analysis of the light curves is discussed in Sect. 4. Bolometric light curves are presented in Sect. 5. The spectra and the analysis of the velocities are shown in Sect. 6. The explosion parameters are estimated in Sect. 7. The results are discussed, summarized and compared with the literature in Sect. 8.

2. The sample

The SN sample presented in this work consists of 60 SNe Ic and 17 SNe Ibc discovered and followed by PTF and iPTF. The clas-

sification of these objects was based on spectroscopy and performed using the Supernova Identification code (SNID, Blondin & Tonry 2007) with the addition of SE SN templates from Modjaz et al. (2014). For illustration, the classification spectra for 10 SNe of the sample are shown in Fig. 1. The objects classified as Type Ibc here are those for which a clear subdivision between Ib and Ic could not be done based on the data quality. This represents the full sample of the PTF + iPTF (hereafter combined into (i)PTF) Type Ic population and our classifications are mostly consistent with those by Fremling et al. (2018). The redshift of the host galaxy has been adopted when available[1]. When this information was not available, the redshift was estimated from the host galaxy lines when detected, otherwise we adopted the best fit from SNID. The redshifts of the sample span the interval $z = 0.004486 - 0.176$. The mean value is $z = 0.049 \pm 0.033$. The redshift distribution is presented in Fig. 2.

The redshift was used to compute the luminosity distance for each SN. We adopted the WMAP 5-year (Komatsu et al. 2009) cosmological parameters $H_0 = 70.5$ km s^{-1} Mpc^{-1}, $\Omega_M = 0.27$, $\Omega_\Lambda = 0.73$ and corrections for peculiar motions (Virgo, GA, Shapley) are included. With these assupmtions, the distance of the sample ranges in the interval D = 19.1 − 847.6 Mpc.
The Milky Way extinction was obtained from Schlafly & Finkbeiner (2011)[2]. The treatment of the host extinction is presented in Sect. 4.3. Our sample was observed mainly in the *r* and *g* bands, with some photometric data also in the *B* and *i* bands for some objects. All the light curves in apparent magnitudes for the 77 SNe are shown in Fig. 3. Among the 60 SNe Ic + 17 SNe Ibc of our sample, 44 were observed before peak in at least one band. In the following analysis we will focus only on these latter 44 objects. These SNe were observed in the *r* band with an average cadence of 3 days and they have been followed with a median coverage of 66 days post peak. The 44 SNe in the sample have a redshift in the interval $z = 0.01377 - 0.176$, the mean value being $z = 0.051 \pm 0.032$. The redshifts for the SNe are highlighted in Fig. 2 and listed in Table 1 where it is specified ifthe redshifts has been obtained with SNID or measure from narrow emission lines. They are all provided with 3 decimals.

This paper is mainly focused on the photometric data of the sample. However, each SN has at least one spectrum obtained by the (i)PTF survey and collaborators. The analysis of these spectra was published in Fremling et al. (2018). This (i)PTF data set of SNe Ic is thus unique given its untargeted nature, its large size, its early coverage, its high cadence and multiband coverage. A detailed analysis of the host galaxies of many of these Type Ic SNe, and of the hosts of the PTF sample of broad lined Type Ic SNe (SNe Ic-BL), was presented by Modjaz, et al. (2020). We compared the classification reported in Modjaz, et al. (2020) with the one we present in this work. We notice that PTF09ps and PTF10bip are presented as Ic/Ic-BL, while PTF11gcj is classified as Ic-BL. We consider these three as SNe Ic as our classification suggested. The analysis of the (i)PTF sample of SNe Ic-BL was published by Taddia et al. (2019). Here we focus on the spectroscopically normal (as opposed to broad lined) SNe Ic. Some of the SNe in our sample have already been studied in other works. SNe PTF09dh, PTF11bli, PTF11jgj, PTF11klg, PTF11rka and PTF12gzk were presented in Prentice et al. (2016). In that work PTF09dh was classified as a SN Ic-BL, but we include it here since we have re-classified it as a spectroscopically-normal SN Ic. We also note that PTF10vgv, presented as a SN Ic in Prentice et al. (2016), is not included in this work since we re-classified it as a SN Ic-BL; therefore, PTF10vgv was presented within the sample of SNe Ic-BL from (i)PTF in Taddia et al. (2019). PTF12gzk was presented and discussed in Ben-Ami et al. (2012); PTF11bov is also known as SN 2011bm and was studied by Valenti et al. (2012) and Taddia et al. (2016); iPTF12gty was presented in De Cia et al. (2017) and also dicussed by Quimby et al. (2018) as a superluminous supernova of Type I (SLSN-I). However, our spectroscopic classification suggests some similarity with a SN Ic so we included it in this work. iPTF15dtg was presented and discussed in Taddia et al. (2016) and late-time data are shown in Taddia et al. (2019). iPTF11mnb was presented in a separate paper as a SN Ic (Taddia et al. 2018a) but it is also discussed in Quimby et al. (2018) as a possible SLSN-I. We include iPTF11mnb in this work since our spectroscopic classification agrees with that of a SN Ic by Taddia et al. (2018a). Finally, iPTF14gqr was presented in De et al. (2018).
We notice that some SNe, spectroscopically classified as normal SNe Ic, show quite broad light curves compared to the bulk of the sample[3]. In order to identify these SNe, the SE SN template presented by Taddia et al. (2015) was used as a reference. The template was shifted and stretched to fit the SN light curve at maximum. The SNe that presented a stretch factor higher than 1.5 were considered as having a broad light curve. The method used and these SNe will be discussed in detail in a coming paper (Karamehmetoglu et al. in prep).

3. Photometric observations and data reduction

SN discovery and early photometric observations were performed with the 48-inch Samuel Oschin Telescope at Palomar Observatory (P48), equipped with the 96 Mpx mosaic camera CFH12K (Rahmer et al. 2008), a Mould *r*-band filter (Ofek et al. 2012) and a *g*-band filter. For 34 SNe in our sample, further follow-up was performed with the automated Palomar 60-inch telescope (P60, Cenko et al. 2006), often in *Bgri* bands. Point spread function (PSF) photometry was obtained on template subtracted images using the Palomar Transient Factory Image Differencing and Extraction (PTFIDE) pipeline (Masci et al. 2017) for P48 data and the FPipe pipeline presented in Fremling et al. (2016) for the P60 data. The photometry was calibrated using Sloan Digital Sky Survey (SDSS) stars (Ahn et al. 2014) in the SN field.

4. Supernova light curves

In Fig. 4 we present the photometric observations in the optical bands available for our SN sample. As mentioned before, we will proceed with our analysis only for those 44 SNe which have been observed before peak. The observed light curves were first corrected for time dilation and K-corrections.

4.1. K-corrections

Most of the SNe were observed in the *r* band and we estimated the observed peak epoch in the *r* band (t_r^{max}) by fitting a polynomial to the *r*-band light curves. The peak epoch is shown with a dashed red line in Fig. 4.

[1] The values refer to the ones available at the NASA/IPAC extragalactic database; http://ned.ipac.caltech.edu
[2] via the NASA/IPAC infrared science archive; https://irsa.ipac.caltech.edu/applications/DUST/
[3] PTF11mnb, PTF11rka, PTF12gty, PTF12gzk, iPTF15dtg, iPTF16flq and iPTF16hgp.

When the peak was observed also (15 objects) or only (4 objects)[4] in the g band, we performed the same fit in this band. The observed phases were corrected by a factor of $(1 + z)$ to account for time dilation in order to obtain the phase in the rest frame. The measured t_r^{max} was used to determine the rest-frame phase of the SN spectra in our sample. The spectra were used to compute average K-corrections for the *Bgri* bands as a function of redshift and time since t_r^{max}. The method we performed has been presented in Taddia et al. (2019) and makes use of all the available spectra of the sample to estimate the K-corrections for every single SN. The main reason to apply this method is the lack of a complete spectral follow-up for most of the SNe of the sample. All the obtained K-corrections were then plotted as a function of the phase and fitted with a second-order polynomial. These fits in the r band are shown in Fig. 5. Overall, we can see that the K-corrections are negligible for most of the objects but when present, at higher z, they are more important at early epochs. We K-corrected all the $g-$ and $r-$band light curves interpolating the above mentioned polynomials at all epochs of the light curve observations. In the following analysis, we will always refer to our K-corrected and time-dilation corrected light curves.

4.2. Light curve shape

We fitted the K-corrected r- and g-band light curves with the function provided by Contardo et al. (2000) to characterise their shapes. This function includes an exponential rise, two Gaussian peaks, and a linear late decline. We included only the first of the two Gaussian peaks in our fit. From this fit it is possible to derive the peak epoch and magnitude, the rise parameter Δm_{-10} as well as the decline parameters Δm_{15}, Δm_{40} and the late linear decline slope. The parameter Δm_{-10} measures how many magnitudes the light curve rises during the 10 rest frame days before peak. Δm_{15} instead represents the decrease in magnitude 15 days after peak and Δm_{40} at 40 days after peak. The results of our fits to the r- and g-band light curves are shown in Fig. 6. In the top panel, each SN is represented individually in the r band while the bottom panel shows the SNe in the g band.

We focus our analysis on the shape of the light curves in the r band. This leads to the exclusion of PTF11hyg, PTF11lmn, iPTF14gao and iPTF15cpq from our analysis since they only show the peak in the g band. In Fig. 7 we present all our 40 SNe together to show the general shape of their light curves in the r band. This highlights the variety of rise and decline rates of the SNe of our sample. Through a Monte-Carlo procedure and simulating N=100 light curves, we estimate the uncertainties on each of the light curve fit parameters according to their photometric uncertainties. The uncertainty on each parameter is represented by the standard deviations of the best fit parameters. These parameters and their estimated uncertainties are reported in Table 2.

Figure 8 suggests a correlation between Δm_{15} and Δm_{-10}, with fast rising SNe also being fast declining. We also show the relation between Δm_{15} and Δm_{40} and the one between Δm_{-10} and Δm_{40} which also seem to suggest a correlation among these parameters. The Δm_{-10} vs Δm_{40} gives a similar relation as Δm_{-10} vs Δm_{15}, implying that the fast rising SNe are the fast declining SNe also at 40 days past peak. The Δm_{15} vs Δm_{40} demonstrates that the SNe that decline fast during the first 2 weeks are also the ones that declined more at these later phases. We performed a Spearman test to quantify these correlations and the p-values are reported in Fig. 8. This test will be performed for all correlations in this work and p-values will be displayed in the plots. The Δm_{-10} and Δm_{40} show a lower p-value than the other two which indicates a stronger correlation, this is most likely due to the presence of few outliers in the other correlations. We estimated the epoch of the peak in g−band for 19 SNe of the sample and compared it with the same estimate for the r−band. We find on average a shift between the peaks at g− and r−band of 4 ± 2 days, with the SN peaking in the g−band first. This is consistent with the estimate of ~ 3 days presented in Taddia et al. (2015).

4.3. Colours and host extinction

We proceed to compute the colour evolution of the SNe, see Fig. 9. For 31 SNe with g- and r-band data available, we corrected for the Milky Way (MW) extinction adopting the MW $E(B - V)$ given in Table 1, assuming $R_V = 3.1$ and a Fitzpatrick (1999) reddening law. We then interpolated the r band to the g-band epochs to obtain the $g - r$ evolution. The colour evolution tends to show an initial rise until approximately 20 days after peak, then it starts a shallow decline (getting bluer) at later epochs (Fig. 9). We estimated the host extinction from spectroscopy from the measurement of the equivalent width of the narrow Na ID absorption line. We followed Taubenberger et al. (2006, their Eq. 1) to get $E(B - V)$ and adopt an uncertainty of $\Delta E(B - V) = 0.2$ mag.
In addition, we used the SN $g - r$ colours to estimate the host extinction, following the method described by Stritzinger et al. (2017). We fit the $g - r$ colours of all the SNe with low-order polynomials, shown as solid lines in Fig. 9. We then estimated the average $E(g - r)$ for each SN in the range between 0 and 20 days since peak by computing the average difference between the fit of the observed $g - r$ and the assumed intrinsic $g - r$ colour. We adopted the $g - r$ template presented in Taddia et al. (2015). The 7 SNe that present broader light curves as mentioned in Sect. 2 require a stretching factor to our template in order to get a good fit (see Karamehmetoglu et al. in prep). We estimated the stretch factor from the ratio between the average Δm_{15} of the sample and the Δm_{15} estimated for the individual SN with broad light curve, and then set the time scale from the ratio of the epochs of the peak in the $g - r$ colour evolution of one broad SN (iPTF16hgp) and one normal (PTF12gzk). We then converted $E(g - r)$ into $E(B - V)_{\rm host}$, assuming $R_V = 3.1$. The uncertainty of the $g - r$ template is included in the uncertainties of the host galaxy extinctions. The uncertainty also takes into account the standard deviation due to the difference between the epochs of the measured colour and the intrinsic $g - r$. We also used the spectra corrected for redshift and Milky Way extinction to build $g - r$ color curves for some SNe[5] for which it was not possible to use the photometry (see bottom panel of Fig. 9). The computed $E(B - V)_{\rm host}$ values are reported in Table 1. We note that for two SNe[6] it was not possible to get a $g - r$ evolution

When we compare the host galaxy extinction estimates obtained from the SN colour comparison to that obtained from the Na ID absorption lines, we notice that the first seems to provide overall higher values (Fig. 10). Both of these methods come with considerable uncertainties and assumptions. We note that some

[4] This was done for 19 SNe namely PTF09dh, PTF11bli, PTF11bov, PTF11hyg, PTF11jgj, PTF11klg, PTF11lmn, PTF11mnb, iPTF12gzk, iPTF12hvv, iPTF14bpy, iPTF14fuz, iPTF14gao, iPTF14gqr, iPTF15acp, iPTF15cpq, iPTF15dtg, iPTF16flq and iPTF16hgp.

[5] In particular, spectra were used for 11 SNe, namely PTF09ut, PTF10bip, PTF10hie, PTF10lbo, PTF10tqi, PTF10yow, PTF10zcn, PTF12cjy, PTF12jxd, iPTF13ab and iPTF13djf

[6] This has been adopted for SNe iPTF13aot and iPTF14jhf.

of our spectra do not have enough signal-to-noise (S/N) close to the Na ID line to properly detect it. On the other hand, the $g-r$ method relies on an intrinsic colour curve template and on assuming homogeneity of the colour evolution for these SNe. In this work we will adopt the extinction estimated from the Na ID, unless otherwise specified. The main reason is that we want to compare our results with those published in the literature, which most often have used this method. However, throughout the analysis we will discuss how some values will be affected if we instead chose the extinction estimated from the second method.

4.4. Absolute magnitudes

We applied the presented corrections; Milky Way and host extinctions, distances and K-corrections, to the light curves to obtain the absolute magnitudes, see Fig. 11. The uncertainty on the absolute magnitudes takes into account the uncertainties due to the host extinction estimates and the photometric errors. In addition, the uncertainty on the distance adds a systematic error of ± 0.15 mag which has not been included in the figure. The distribution of the r-band absolute magnitudes at peak is shown in Fig. 12. Our r-band magnitudes span the interval −15.45 to −19.73 mag when the host extinction has not been accounted for, giving an average of $< M_r^{\rm peak} >= -17.50 \pm 0.82$ mag. It ranges from −15.54 to −19.81 mag when the host extinction from Na ID is included, with an average of $< M_r^{\rm peak} >= -17.71 \pm 0.85$ mag. If we instead consider the extinction estimates from $g-r$, the interval is −16.91 to −19.84 mag and an average of $< M_r^{\rm peak} >= -18.07 \pm 0.84$ mag. All values for each SN in the sample are reported in Table 3. We notice how PTF12gty is the brightest SN in the sample with an absolute peak magnitude of −19.81.
The absolute magnitude ranges available in the literature are $M_r^{\rm peak} = -18.26 \pm 0.21$ mag (Taddia et al. 2015); $M_r^{\rm peak} = -17.64 \pm 0.26$ mag (Taddia et al. 2018b) and $M_R^{\rm peak} = -18.3 \pm 0.6$ mag (Drout et al. 2011). The average peak magnitude in the r band estimated for our sample is thus in agreement with the ones from the literature. We compared these values also with the (i)PTF sample of SNe Ic-BL (Taddia et al. 2019) where the average peak magnitude is -18.7 ± 0.7 mag. Our SNe Ic are on average fainter than the SNe Ic-BL. We investigated the absolute r-band magnitude peak versus $\Delta m_{15}(r)$ behaviour, to test if there is a Phillips-like relation as for SNe Ia (Phillips 1993). We found that SNe Ic do not show any clear such correlation (see Fig. 13). This is in agreement with previous studies on SE SNe (Prentice et al. 2016; Lyman et al. 2016; Drout et al. 2011). Also a dedicated study on SNe Ic-BL has shown that there is no evidence for such a correlation (Taddia et al. 2019).
For SNe having data more than 70 days past peak, we also measured the slope at late epochs. We investigated the $\Delta m_{15}(r)$ versus the slope and we did not see any clear correlation. Our g-band peak magnitudes for 19 SNe span the interval −15.86 to −18.91 mag when the host extinction is not taken into account and it ranges from −17.10 to −19.51 mag when included, with an average value of -17.99 ± 0.69. Finally, if we consider the extinction we get from the $g-r$ method the interval is −17.04 to −19.44 mag. The average value for the peak magnitude in the g−band is in agreement with the -17.28 ± 0.24 found by Taddia et al. (2018b).

4.5. Explosion epochs and rise times

In order to estimate the explosion epochs for each SN, we compare their r-band light curves with the r-band light curve of iPTF13djf. This supernova has a good photometric coverage and well determined explosion epoch, with a limit on the discovery date of only ±1 day. Since the explosion epoch of iPTF13djf is well constrained, as is the peak epoch in the r band, we use it as a template and the stretch of the best fit allows us to infer the explosion epoch for all other SNe in the sample. The light curve of iPTF13djf is stretched in time and shifted in magnitude to fit our SN light curves until +30 days post peak. The estimated explosion epoch were checked against the pre-explosion limits for consistency. We adopted ±2 days as a conservative estimate of the uncertainties on the explosion epochs.
In a few cases when this method did not give results consistent with the pre-explosion limits, we assume the last non-detection as the explosion epoch.[7] When an estimate for the SN explosion epoch was available from literature, we adopted the latter as our explosion epoch. This was the case for PTF11mnb (Taddia et al. 2018a), iPTF14gqr (De et al. 2018) and iPTF15dtg (Taddia et al. 2016). The best fits and the obtained explosion epochs are shown in Fig. 15. The inferred explosion epochs are reported in Table 4. The explosion epochs and the epochs of the maximum in r band allow us to compute the rest-frame r-band rise time, these are provided in Table 4.

5. Construction of the Bolometric Light curves

Modeling of the bolometric light curves can help derive parameters on the supernova progenitors and on the explosion physics. To accomplish this, we need to estimate the explosion epochs and construct the bolometric light curves.

5.1. Bolometric lightcurves

Due to the lack of a complete multiband coverage, in particular at early epochs, we used the absolute r-band light curves and the fit of the $g-r$ colour evolution to compute the bolometric light curves, making use of the bolometric corrections for SE SNe presented by Lyman et al. (2014). In this way we are able to create the bolometric light curves covering all the phases. The bolometric light curves of 12 SNe[8] were built applying the bolometric correction directly to the g band, which is what is needed for the method of Lyman et al. (2014). For the other 30 SNe we interpolate the g band from the r band and then applied the bolometric correction. Only for iPTF13aot and iPTF14jhf were we unable to build a bolometric light curve due to a lack of $g-r$ evolution and these are therefore excluded from the analysis. The final bolometric light curves as a function of days since explosion are shown in Fig. 16. The systematic uncertainties due to the bolometric correction (0.076 mag) and on the distance (0.15 mag) are not included in the errors of each bolometric light curve.

5.2. Analysis of the bolometric light curve shape

We fit the bolometric light curves with the Contardo function also used in Sect. 4.2. The best fits are shown in the plot as solid lines in Fig. 16. Following the same analysis as for the r band, this allow us to measure some properties of the shape of the bolometric light curves, such as the peak magnitude, the peak epoch, Δm_{-10}, Δm_{15} as well as the linear decline slope. We

[7] We assumed the last non detection as explosion epoch for PTF09dh, PTF10hfe, PTF10tqi, PTF10zcn and PTF12gzk.
[8] PTF11bli, PTF11bov, PTF11hyg, PTF11lmn, PTF11mnb, iPTF14fuz, iPTF14gao, iPTF14gqr, iPTF15acp, iPTF15cpq, iPTF15dtg and iPTF16hgp.

present all these parameters in Table 2. Our sample peak magnitudes span the interval −16.10 to −19.78 mag giving an average of $< M_{bol}^{\rm peak} >= -17.62 \pm 0.94$ mag. We investigated the same correlations as for the *r* band, they are presented in Fig. 18. We find the same correlations as for the r−band. We also estimated the rise times for the bolometric light curves in the same way as we did for the *r* band and these values are reported in Table 4.

6. Supernova spectra

This work is focused on the photometric analysis of a sample of SNe Ic, a study of the spectroscopic properties was presented in Fremling et al. (2018). However, one of the aims is to use these light curves to estimate explosion parameters (Sect. 7), and in order to break the degeneracy between explosion energy and ejecta mass such an analysis requires an estimate of the photospheric velocity. This will be presented here.

6.1. Photospheric velocities

In order to determine the photospheric velocities for the SNe in our sample we estimate the expansion velocities using the Fe II λ5169 line. These velocities were evaluated from the minima of the P-Cygni profile of the Fe II λ5169 for all the available spectra. For six SNe[9] it was not possible to estimate the Fe II λ5169 velocities as the S/N of the spectra were too low. We also excluded, for now, PTF12gzk as it is known from the literature to be a high velocity SN (Horesh et al. 2013) and we here aim to build up a general trend for normal SNe Ic. The time evolution of the Fe II λ5169 velocities for the 37 SNe so selected is presented in Fig. 14, where the magenta solid line shows the power law which best represents the trend shown by the overall velocities. This power-law trend for Fe II λ5169 is in agreement with the trend found by Taddia et al. (2018b) for SE SNe, the functional form we found is $v(t) \propto (t - t_0)^{-0.30}$, where t_0 represents the explosion epoch.
In Fig. 14 we also compare the Fe II λ5169 evolution with the trend found by Modjaz et al. (2016). Their velocities are lower than our best fits at early epochs. A polynomial fit is also presented

The photospheric velocities required to estimate the explosion parameters are the Fe II λ5169 velocities at peak. This is not available for every SN in the sample. We then use the general trend found for the overall sample and assume that it represents the velocity evolution for each individual SN. We thus apply our power-law as a template to every SN, shifting it to the available velocity values for the individual SNe. Once it has been shifted, we can extrapolate the value of the Fe II λ5169 velocity at peak. We estimate the average velocity at peak of the SNe of our sample and adopted this average value to be the velocity for the six SNe for which we were unable to measure the Fe II λ5169 velocity. The power-law method is also applied to the velocities estimated for PTF12gzk, as these velocities show a similar trend but at higher values. The uncertainties on the peak velocity were assumed to be 10% of the estimated value. In this way we get a full set of velocities at peak for the 42 SNe of the sample that will be used in Sect. 7 to estimate the explosion parameters. The estimated velocities at peak are presented in Table 5. We notice how PTF10bip presents higher velocities compared to the average of the sample, this could explain the Ic/Ic-BL classification from Modjaz, et al. (2020).

[9] PTF09dh, PTF09ut, PTF11jgj, PTF12cjy, PTF12fgw and iPTF13djf.

7. Explosion parameters

In order to estimate the explosion parameters, we fit the bolometric light curves with an Arnett model (Arnett 1982). The method we followed to perfom the fit is presented in Taddia et al. (2018b). We performed the fits on the early epochs of the light curves, $\lesssim 60$ days after peak, during the photospheric phase of the SNe. The parameters we can estimate from this modelling are the ^{56}Ni mass ($M_{^{56}\rm Ni}$), the kinetic energy of the explosion (E_K) and the ejecta mass (M_{ej}). We assume that the SN ejecta have spherical symmetry and uniform density; we also use $E/M = (3/10)V^2$, where V is the appropriate ejecta velocity at peak as discussed in Sect. 6.1. We furthermore assumed a constant opacity $\kappa = 0.07$ cm^2 g^{-1}, as is often done in the literature on SE SN samples. The Arnett fit for the SNe of the sample is shown in Fig. 17. The estimated values for $M_{^{56}\rm Ni}$, M_{ej}, and E_K are listed in Table 6. The uncertainties on $M_{^{56}\rm Ni}$ is mostly due to the uncertainty on the SN distances. The uncertainties on M_{ej} and E_K instead depend mostly on the uncertainty on the expansion velocity. We notice that the Arnett fit gives a particular high value of $M_{^{56}\rm Ni}$ for PTF12gty ($\sim 3\ M_\odot$). We conclude that this SN, which has been an outlier for most of the analysis in this work, is most likely a SLSN, as discussed in De Cia et al. (2017); Quimby et al. (2018). It will therefore be excluded from the estimates of the average explosion parameters. This reduces the final sample of SNe Ic to 41. We then obtained average values of $< M_{ej} >= 4.39 \pm 0.31\ M_\odot$, $< E_K >= 1.71 \pm 0.16$ foe (1 foe = 10^{51} erg), and $< M_{^{56}\rm Ni} >= 0.19 \pm 0.05\ M_\odot$ where the errors are the weighted errors. In Fig. 19 we plot each estimated parameter against the others. We identify a correlation between M_{ej} and E_K (see bottom panel). We also notice a correlation between the M_{ej} and $M_{^{56}\rm Ni}$, and between $M_{^{56}\rm Ni}$ and E_K. The probability density function (PDF) of the three explosion parameters are shown in Fig. 20. It shows, for all parameters, that most of the SNe are distributed around a common peak, but there are also evidence for distributions towards higher values in all three parameters. In Sect. 2, we mentioned that 6 SNe show broader light curves compared to the rest of the sample, which will be discussed separately (Karamehmetoglu et al., in prep). If we exclude the SNe that show broad light curves[10] we obtain averages $< M_{ej} >= 3.54 \pm 0.30\ M_\odot$, $< E_K >= 1.50 \pm 0.15$ foe, and $< M_{^{56}\rm Ni} >= 0.15 \pm 0.06\ M_\odot$ where again the errors represent the weighted errors. Excluding the 6 SNe with broad light curves clearly gives lower average values for M_{ej} and $M_{^{56}\rm Ni}$. If we furthermore exclude from the average the peculiar fast ultrastripped iPTF14gqr (De et al. 2018) we get $< M_{ej} >= 3.94 \pm 1.07\ M_\odot$, $< E_K >= 1.20 \pm 0.19$ foe , and $< M_{^{56}\rm Ni} >= 0.15 \pm 0.05\ M_\odot$. These average values, now based on 34 normal SNe Ic, are still consistent with the previous ones within the uncertainties.

8. Discussion and Conclusions

PTF and iPTF allowed for a larger, untargeted, and more homogeneous data set as compared with other SN Ic samples, and for this sample we also have good constraints on the explosion epochs. We investigated two different methods to estimate the host extinction. First we inspected the spectra to look for Na ID absorption and using Taubenberger et al. (2006) we calculated the $E(B-V)$. This method is dependent on the S/N and resolution of the spectrum. The second method is based on the $g-r$ colour evolution and is described in Stritzinger et al. (2017). This

[10] PTF11mnb, PTF11rka, PTF12gzk, iPTF15dtg, iPTF16flq and iPTF16hgp.

method assumes that SE SNe show an intrinsically homogeneous colour evolution in the range 0 – 20 days past peak. We compare the results of these methods in Fig. 10, which shows that the extinction estimated through the colour evolution is generally higher. We adopted the extinction estimated from the Na ID for the overall analysis, but also compared how the peak magnitudes would change if we had adapted the other method. The average absolute peak magnitude is $< M_r^{\rm peak} >= -17.71 \pm 0.85$ mag. In case we adopt the extinction from the $g - r$ evolution we get $< M_r^{\rm peak} >= -18.03 \pm 0.79$ mag. The effect on the overall peak magnitude distribution are shown in Fig. 12, where accounting for higher extinction as suggested by the Stritzinger method shifts the overall sample is towards brighter magnitudes.

We investigated the light curve shape in both the r band and for the bolometric light curves. We looked for correlations among the main parameters: magnitude at peak, Δm_{-10}, Δm_{15}, Δm_{40} and slope. In both cases, we found a correlation between Δm_{15} and Δm_{-10}, implying that slow-rising SNe are also slow decliners. We see a correlation also among Δm_{40} vs Δm_{15} and for Δm_{40} vs Δm_{-10}. We fitted the bolometric light curves with an Arnett model (Arnett 1982) to estimate the explosion parameters. We obtained average values of $< M_{ej} >= 4.39 \pm 0.31\ M_\odot$, $< E_K >= 1.71 \pm 0.16$ foe, and $< M_{^{56}\rm Ni} >= 0.19 \pm 0.05\ M_\odot$, when including all the 41 SNe Ic for which we could estimate these parameters. We searched for correlations among the explosion parameters and identify a correlation between M_{ej} and E_K. We also notice a correlation between the M_{ej} and $M_{^{56}\rm Ni}$, and between $M_{^{56}\rm Ni}$ and E_K.

8.1. Comparison with the literature

Some of the SNe in this sample have already been discussed in the literature, and we will here compare our results with these available in those publications. SNe PTF09dh, PTF11bli, PTF11jgj, PTF11klg, PTF11rka and PTF12gzk were presented in Prentice et al. (2016). Our estimated $M_{^{56}\rm Ni}$ values for these SNe are in agreement with the ones provided in their work. PTF12gzk is discussed in Ben-Ami et al. (2012), in which they noted that this SN showed some aspects inbetween SNe Ic and SNe Ic-BL. They conclude that the mass of the progenitor star is $25 - 35\ M_\odot$. We also get quite high values for the ejecta mass which points towards a massive progenitor star, comparable with the values from Ben-Ami et al. (2012). PTF11bov is also known as SN 2011bm and was presented in Valenti et al. (2012) where they infer an initial mass for the progenitor of $30 - 50\ M_\odot$. The explosion parameters we derive are close to the lower end of the interval they present in their work. iPTF15dtg was first introduced in Taddia et al. (2016) and investigated further in Taddia et al. (2019). In their first work they concluded that the peculiar long rise of this SN was most likely due to an extended envelope around the progenitor star, which they claim was a massive ($> 35\ M_\odot$) Wolf-Rayet star. The explosion parameters we estimated using the Arnett model are somewhat consistent with their lower values. In the subsequent paper, they accounted for additional peculiar behaviour of the SN at late times, which was explained by a combination of radioactive and magnetar powering which leads to a lower estimate of M_{ej} when compared with our estimate.

iPTF14gqr was presented in De et al. (2018) where they concluded that the best interpretation for this fast event is a ultra-stripped SN. We also obtained low values for the explosion parameters, in agreement with the scenario presented in De et al. (2018). iPTF11mnb was presented in a separate paper as a SN Ic from a massive progenitor ($85\ M_\odot$; Taddia et al. 2018a). Our estimates also show high values for the explosion parameters pointing towards a massive progenitor star. iPTF12gty was classified as a SLSN by Quimby et al. (2018) and further investigated by De Cia et al. (2017). Our spectral classification was pointing towards a SN Ic classification but this SN is a clear outlier in the sample in many ways. In particular, when applying the Arnett fit to estimate the explosion parameters we get a very high value of the ^{56}Ni mass. We therefore conclude that iPTF12gty is most likely a super-luminous SN. Our r-band absolute magnitudes span the interval -15.54 to -19.81 mag, with an average of $< M_r >= -17.71 \pm 0.85$ mag. The ranges available in the literature are $M_r^{\rm peak} = -18.26 \pm 0.21$ mag (Taddia et al. 2015); $M_r^{\rm peak} = -17.64 \pm 0.26$ mag (Taddia et al. 2018b) and $M_R^{\rm peak} = -18.3 \pm 0.6$ mag (Drout et al. 2011). The average peak magnitude in the r band estimated for our sample is in agreement with the ones from literature. We compared our values also with the (i)PTF sample of SNe Ic-BL (Taddia et al. 2019) where the peak magnitudes show a brighter average of -18.7 ± 0.7 mag. We analysed the shapes of the r-band light curves and of the bolometric light curves, searching for correlations among the different parameters. We identified a correlation in the r band between Δm_{15} and Δm_{-10} which is in agreement with the results from-Taddia et al. (2019); Drout et al. (2011). We note that the fact that the fast risers are also the fast decliners is not trivially true. There could well be different physical circumstances determining the rise and the decline from peak, for example the mixing out of radioactive nickel will affect the steepness of the rising light curve whereas the time scale for the decline may be more determined by the ejecta mass and composition that sets the diffusion time. We did not find any Philips-like relation and this is in agreement with previous works (Taddia et al. 2019; Lyman et al. 2016; Drout et al. 2011).

We compared the estimated average values for the explosion parameters of the 41 (i)PTF SNe Ic with the ones available in the literature. Drout et al. (2011) presented $M_{^{56}\rm Ni}$ values for 9 SNe Ic. In Cano et al. (2013) the explosion parameters for 13 SNe Ic are presented. Taddia et al. (2015) analysed three events, while the Lyman et al. (2016) sample contains 8 SNe Ic. A total number of 13 SNe Ic was presented in Prentice et al. (2016). Taddia et al. (2018b) presented 11 SNe Ic and in Prentice et al. (2019) three SNe Ic are included. Our (i)PTF sample with 41 SNe Ic therefore by far represents the largest sample of SNe Ic available where the explosion parameters have been estimated. We estimated the cumulative distribution functions (CDF) of the explosions parameters, and compared it to the available studies in the literature. The results of these comparisons are shown in Fig. 21. We also report the averages values and their standard deviations for the estimated explosion parameters from the different samples in Table 7. We searched for correlations among the explosions parameters (see Fig. 19), and identify a correlation between M_{ej} and E_K. We also notice correlations between M_{ej} and $M_{^{56}\rm Ni}$, and between $M_{^{56}\rm Ni}$ and E_K. These correlations were also observed in other SE SN studies (Taddia et al. 2019, 2018a; Lyman et al. 2016).

8.2. Implications for progenitors

The PDF of the different explosion parameters are shown in Fig. 20. The E_K shows a first strong peak for energies lower than 3 foe and the $M_{^{56}\rm Ni}$ distribution shows a clear peak at values lower than $0.3\ M_\odot$ The PDF of the M_{ej} shows a first peak for values lower than $5\ M_\odot$ and shows indication for additional

peak(s) towards higher mass. A similar analysis for M_{ej} was presented in Lyman et al. (2016) and from a comparison with expectations from models they concluded that since the peak of ejecta masses is rather low, this indicates that the majority of SE SNe originate from not too massive stars. Moreover, since such stars are unable to get rid of all of their outer hydrogen and helium layers soley from mass-loss from winds, they must likely have been born and stripped in a binary system. The trend we see here for our larger sample would lead to a similar conclusion. We notice that the PDF presented in Lyman et al. (2016) did not show a very pronounced secondary peak. This is due to the presence of SNe with a broad light curves which could arise from more massive star progenitors. These SNe will be discussed into more detail in Karamemehtoglu et al., (in prep.).

We have presented the sample of Type Ic supernovae collected by (i)PTF over a period of $\sim$ 7 years. The final sample of SNe that also have pre−peak photometry is made up of 44 objects, which we analyse in terms of light-curve and explosion parameters. This is the largest such sample to date. Our main results confirm trends seen in previous articles based on smaller and less homogenous samples. Although our data are not always fantastic for individual SNe, the bulk sample provides a good picture of the overall properties of this class of extremely stripped supernovae.

The moderate released ejecta masses remain a challenge for scenarios involving single very massive stars, as already proposed by Lyman et al. (2016), and corroborate discussions on the need for binary star evolution to produce most of the Type Ic SNe. Indications for a population of more massive progenitors are also seen. The ejected masses of radioactive nickel are $\sim 0.2 M_{\odot}$, which is more than current explosion models Ertl, et al. (2020) can easily accomplish.

There is hope for better understanding of these explosions from the observational perspective. The Zwicky Transient Facility Bellm, et al. (2019) that has taken over on the P48 telescope after (i)PTF enable superior light curves also of Type Ic SNe. Over the first years, this survey has already observed almost 100 Type Ic SNe, and a fair fraction of these have better sampled LC:s than the sample we have presented here. We look forward to analysing these new data.

9. Acknowledgements

The Oskar Klein Centre was funded by the Swedish Research Council. C.B. gratefully acknowledge support from the Knut and Alice Wallenberg Foundation, and from the Wennergren Foundation (PI JS).

The intermediate Palomar Transient Factory project is a scientific collaboration among the California Institute of Technology, Los Alamos National Laboratory, the University of Wisconsin, Milwaukee, the Oskar Klein Center, the Weizmann Institute of Science, the TANGO Program of the University System of Taiwan, and the Kavli Institute for the Physics and Mathematics of the Universe. LANL participation in iPTF is supported by the US Department of Energy as a part of the Laboratory Directed Research and Development program.

The data presented herein were obtained in part with ALFOSC, which is provided by the Instituto de Astrofisica de Andalucia (IAA) under a joint agreement with the University of Copenhagen and NOTSA.

References

Ahn, C. P., Alexandroff, R., Allende Prieto, C., et al. 2014, ApJS, 211, 17
Arnett, W. D. 1982, ApJ, 253, 785
Barbarino, C., Botticella, M. T., Dall'Ora, M., et al. 2017, MNRAS, 471, 2463
Begelman, M. C., & Sarazin, C. L. 1986, ApJ, 302, L59
Bellm E. C., et al., 2019, PASP, 131, 018002
Ben-Ami, S., Gal-Yam, A., Filippenko, A. V., et al. 2012, ApJ, 760, L33
Bersten, M. C., Benvenuto, O. G., Folatelli, G., et al. 2014, AJ, 148, 68
Blondin, S., & Tonry, J. L. 2007, ApJ, 666, 1024
Cano, Z. 2013, MNRAS, 434, 1098
Cenko, S. B., Fox, D. B., Moon, D.-S., et al. 2006, PASP, 118, 1396
Contardo, G., Leibundgut, B., & Vacca, W. D. 2000, A&A, 359, 876
De, K., Kasliwal, M. M., Ofek, E. O., et al. 2018, Science, 362, 201
De Cia, A., Gal-Yam, A., Rubin, A., et al. 2017, arXiv:1708.01623
Drout, M. R., Soderberg, A. M., Gal-Yam, A., et al. 2011, ApJ, 741, 97
Eldridge, J. J., Fraser, M., Maund, J. R., & Smartt, S. J. 2015, MNRAS, 446, 2689
Eldridge, J. J., Fraser, M., Smartt, S. J., Maund, J. R., & Crockett, R. M. 2013, MNRAS, 436, 774
Ertl T., Woosley S. E., Sukhbold T., Janka H.-T., 2020, ApJ, 890, 51
Filippenko, A.V. 1997, ARAA, 35, 309
Fitzpatrick, E. L. 1999, PASP, 111, 63
Fremling, C., Sollerman, J., Kasliwal, M. M., et al. 2018, A&A, 618, A37
Fremling, C., Sollerman, J., Taddia, F., et al. 2016, A&A, 593, A68
Fremling, C., Sollerman, J., Taddia, F., et al. 2014, A&A, 565, A114
Horesh, A., Kulkarni, S. R., Corsi, A., et al. 2013, ApJ, 778, 63
Karamehmetoglu, E., Taddia, F., Sollerman, J., et al. 2017, A&A, 602, A93
Komatsu, E., Dunkley, J., Nolta, M. R., et al. 2009, ApJS, 180, 330
Kulkarni, S. R. 2013, The Astronomer's Telegram, 4807, 1
Law, N. M., Kulkarni, S. R., Dekany, R. G., et al. 2009, PASP, 121, 1395
Lyman, J. D., Bersier, D., & James, P. A. 2014, MNRAS, 437, 3848
Lyman, J. D., Bersier, D., James, P. A., et al. 2016, MNRAS, 457, 328
Masci, F. J., Laher, R. R., Rebbapragada, U. D., et al. 2017, PASP, 129, 014002
Modjaz M., et al., 2020, ApJ, 892, 153
Modjaz, M., Liu, Y. Q., Bianco, F. B., & Graur, O. 2016, ApJ, 832, 108
Modjaz, M., Blondin, S., Kirshner, R. P., et al. 2014, AJ, 147, 99
Ofek, E. O., Laher, R., Law, N., et al. 2012, PASP, 124, 62
Phillips, M. M. 1993, ApJ, 413, L105
Podsiadlowski, P., Joss, P. C., & Hsu, J. J. L. 1992, ApJ, 391, 246
Prentice, S. J., Ashall, C., James, P. A., et al. 2019, MNRAS, 485, 1559
Prentice, S. J., Mazzali, P. A., Pian, E., et al. 2016, MNRAS, 458, 2973
Quimby, R. M., De Cia, A., Gal-Yam, A., et al. 2018, ApJ, 855, 2
Rahmer, G., Smith, R., Velur, V., et al. 2008, Proc. SPIE, 7014,
Rau, A., Kulkarni, S. R., Law, N. M., et al. 2009, PASP, 121, 1334
Schlafly, E. F., & Finkbeiner, D. P. 2011, ApJ, 737, 103
Smartt, S. J. 2009, ARA&A, 47, 63
Stritzinger, M. D., Taddia, F., Burns, C. R., et al. 2017, arXiv:1707.07615
Taddia, F., Sollerman, J., Fremling, C., et al. 2019, A&A, 621, A71
Taddia, F., Sollerman, J., Fremling, C., et al. 2019, A&A, 621, A64
Taddia, F., Stritzinger, M. D., Bersten, M., et al. 2018, A&A, 609, A136
Taddia, F., Sollerman, J., Fremling, C., et al. 2018, A&A, 609, A106
Taddia, F., Fremling, C., Sollerman, J., et al. 2016, A&A, 592, A89
Taddia, F., Sollerman, J., Leloudas, G., et al. 2015, A&A, 574, A60
Taubenberger, S., Pastorello, A., Mazzali, P. A., et al. 2006, MNRAS, 371, 1459
Valenti, S., Taubenberger, S., Pastorello, A., et al. 2012, ApJ, 749, L28
Wheeler, J. C., & Levreault, R. 1985, ApJ, 294, L17
Woosley, S. E., Langer, N., & Weaver, T. A. 1995, ApJ, 448, 315
Yoon, S.-C., Woosley, S. E., & Langer, N. 2010, ApJ, 725, 940

Table 1. List of the 44 SNe Ic in the sample used in this work with their coordinates, redshifts, distances and extinction estimates.

SN	Type	RA	Dec	z	Distance modulus	Distance	$E(B-V)_{MW}$	$E(B-V)_{host}$ from Na I D	$E(B-V)_{host}$ from $g-r$
		(h m s)	(° ' ")		(mag)	(Mpc)	(mag)	(mag)	(mag)
09dh	Ic	14:44:42.07	+49:43:44.9	0.070[1]	37.48	313.91	0.0213	0.16	0.36
09ut	Ibc	14:12:07.64	+74:45:46.0	0.042[1]	36.33	184.50	0.0260	0.00	0.63
10bip	Ic	12:34:10.52	+08:21:48.5	0.051	36.77	225.55	0.0159	0.06	0.00
10hfe	Ic	12:32:05.16	+66:24:23.9	0.049	36.68	216.38	0.0157	0.00	0.00
10hie	Ic	17:02:27.71	+28:31:57.6	0.067[2]	37.38	299.81	0.0464	0.02	0.84
10lbo	Ic	12:59:14.79	+61:27:02.2	0.053[2]	36.85	234.74	0.0138	0.00	0.00
10osn	Ic	23:23:07.98	+17:30:29.1	0.038	36.11	166.43	0.0361	0.00	0.15
10tqi	Ic	23:20:47.73	+18:54:17.3	0.038	36.14	169.13	0.0347	0.16	0.46
10yow	Ic	21:54:23.30	+15:09:20.7	0.024	35.13	106.34	0.0902	0.18	0.56
10zcn	Ic	23:19:14.39	+26:03:11.6	0.020[1]	34.78	90.25	0.0794	0.12	1.64
11bli	Ibc	14:02:16.18	+33:39:41.5	0.034	35.88	149.80	0.0124	0.10	1.27
11bov	Ic	12:56:53.94	+22:22:28.1	0.021	34.90	95.62	0.0289	0.05	0.00
11hyg	Ic	23:27:57.34	+08:46:38.0	0.029	35.50	125.81	0.0509	0.10	0.66
11jgj	Ic	16:31:32.35	+62:06:09.5	0.040[2]	36.22	175.45	0.0257	0.22	0.68
11klg	Ic	22:07:09.92	+06:29:08.7	0.026	35.31	115.15	0.0754	0.00	0.72
11lmn	Ibc	17:30:16.33	+26:59:34.0	0.090[2]	38.07	411.33	0.0439	0.00	0.00
11mnb	Ic	00:34:13.25	+02:48:31.4	0.060[2]	37.14	268.51	0.0157	0.08	0.21
11mwk	Ibc	21:35:01.39	+00:07:16.0	0.121[2]	38.76	564.78	0.0457	0.02	0.00
11rka	Ic	12:40:44.87	+12:53:21.4	0.074[2]	37.62	334.70	0.0295	0.08	0.76
12dtf	Ic	17:14:43.72	+45:18:19.0	0.061[2]	36.43	193.58	0.0347	0.00	0.00
12dcp	Ic	16:12:56.12	+32:30:43.2	0.031	35.65	134.74	0.0204	0.00	0.98
12cjy	Ic	14:34:27.31	+51:49:03.7	0.044	37.17	271.77	0.0082	0.04	0.89
12fgw	Ic	15:53:27.12	+33:21:04.2	0.055	36.94	243.96	0.0287	0.00	0.00
12gty	Ic	16:01:15.23	+21:23:17.4	0.176[1]	39.64	847.56	0.0589	0.03	0.11
12gzk	Ic	22:12:41.53	+00:30:43.1	0.013[2]	33.86	59.20	0.0432	0.14	0.53
12hvv	Ic	21:45:46.45	-00:03:25.1	0.029[2]	35.50	126.14	0.0715	0.08	1.81
12jxd	Ic	09:37:29.82	+23:09:50.2	0.025	35.21	110.18	0.0258	0.32	1.10
12ktu	Ic	04:26:20.58	-10:06:12.5	0.031	35.65	135.05	0.0567	0.08	0.87
13ab	Ic	12:38:12.51	+07:09:02.0	0.048	36.63	211.81	0.0183	0.04	0.00
13aot	Ic	13:18:26.09	+31:28:09.9	0.018	34.53	80.65	0.0103	0.04	–
13cuv	Ic	01:53:20.32	+35:50:19.3	0.049[2]	36.48	198.13	0.0605	0.02	0.68
13dht	Ic	23:44:58.88	+09:55:24.8	0.040[2]	36.22	175.45	0.0658	0.06	0.50
13djf	Ic	23:33:38.73	+08:48:44.6	0.021	34.70	87.07	0.0690	0.03	1.47
14bpy	Ic	15:33:08.66	+17:17:53.3	0.045[1]	36.48	198.13	0.0361	0.00	0.00
14gao	Ic	00:57:40.21	+43:47:35.2	0.018	36.43	193.58	0.0688	0.04	0.01
14gqr	Ic	23:33:27.95	+33:38:46.1	0.063[2]	34.45	77.64	0.0800	0.41	1.41
14fuz	Ibc	01:05:30.18	+02:51:42.0	0.044	37.24	281.09	0.0235	0.00	0.00
14jhf	Ibc	08:00:33.06	+18:15:35.9	0.053[2]	36.90	239.35	0.0202	0.31	–
14ym	Ic	17:46:40.45	+58:38:11.1	0.031	35.68	136.83	0.0400	0.15	0.85
15acp	Ic	14:53:56.34	+59:02:51.4	0.138[2]	39.06	648.56	0.0094	0.13	0.41
15cpq	Ibc	00:13:43.16	+00:09:43.2	0.066[2]	37.35	295.12	0.0238	0.10	0.28
15dtg	Ic	02:30:20.05	+37:14:06.7	0.052[2]	36.83	231.98	0.0549	0.00	0.59
16flq	Ibc	00:28:36.54	-01:33:03.3	0.059[1]	37.13	266.65	0.0190	0.24	0.17
16hgp	Ic	00:12:06.41	+32:11:50.9	0.079[2]	37.76	356.57	0.038	0.00	0.36

[1]Redshift estimated from SNID

[2]Redshift estimated from narrow host line

Table 2. Parameters for the analysis of the lightcurve shape in the *r* band for the 40 SNe, uncertainties are in parentesis.

SN	t_r^{max} (JD)	m_r^{peak} (mag)	$\Delta m_{15}(r)$ (mag)	$\Delta m_{-10}(r)$ (mag)
09dh	2454954.43(0.11)	18.65(0.01)	0.62(0.02)	0.71(0.08)
09ut	2455014.29(1.97)	19.91(0.11)	0.20(0.05)	—
10bip	2455231.72(0.12)	19.38(0.05)	0.43(0.01)	—
10hfe	2455341.19(1.41)	20.00(0.11)	0.50(0.03)	—
10hie	2455336.27(0.01)	19.71(0.08)	0.73(0.05)	—
10lbo	2455377.10(0.50)	19.37(0.07)	0.29(0.01)	0.26(0.01)
10osn	2455398.18(0.70)	19.27(0.07)	0.65(0.01)	—
10tqi	2455443.58(0.30)	19.05(0.08)	0.55(0.02)	0.80(0.04)
10yow	2455480.75(0.88)	18.61(0.12)	0.84(0.05)	1.29(0.17)
10zcn	2455487.63(0.21)	18.42(0.05)	0.65(0.02)	—
11bli	2455646.01(1.04)	18.61(0.05)	0.49(0.03)	—
11bov	2455685.29(0.16)	16.85(0.03)	0.19(0.01)	0.07(0.002)
11jgj	2455786.34(0.88)	19.03(0.05)	0.37(0.08)	0.34(0.04)
11klg	2455809.06(0.03)	18.25(0.01)	0.76(0.01)	0.62(0.05)
11mnb	2455861.35(1.17)	18.86(0.02)	0.37(0.13)	0.19(0.07)
11mwk	2455829.79(0.93)	20.48(0.19)	0.48(0.05)	—
11rka	2455930.57(0.43)	19.11(0.03)	0.14(0.02)	0.11(0.01)
12cjy	2456026.13(0.90)	19.59(0.06)	0.53(0.04)	—
12dcp	2456048.16(1.59)	18.74(0.07)	0.32(0.06)	0.07(0.03)
12dtf	2456056.13(0.49)	19.64(0.05)	0.41(0.02)	0.38(0.03)
12fgw	2456093.36(0.06)	19.30(0.08)	1.52(0.05)	1.45(0.05)
12gty	2456171.93(0.80)	20.08(0.05)	0.41(0.06)	0.11(0.02)
12gzk	2456152.44(0.03)	15.37(0.01)	0.46(0.03)	0.42(0.01)
12hvv	2456165.97(0.12)	18.34(0.02)	0.14(0.01)	1.21(0.07)
12jxd	2456229.95(0.31)	19.33(0.07)	0.67(0.03)	—
12ktu	2456245.37(0.20)	19.37(0.03)	1.06(0.14)	0.89(0.13)
13ab	2456333.82(0.87)	19.85(0.06)	0.39(0.02)	—
13aot	2456416.55(0.35)	17.88(0.04)	0.43(0.01)	0.16(0.01)
13cuv	2456537.31(0.29)	19.34(0.07)	0.43(0.02)	0.32(0.01)
13dht	2456551.36(0.89)	19.49(0.07)	0.51(0.04)	—
13djf	2456557.86(0.61)	19.40(0.09)	0.60(0.04)	0.65(0.14)
14bpy	2456835.60(0.68)	18.89(0.08)	—	1.05(0.14)
14fuz	2456927.38(0.05)	19.05(0.04)	0.43(0.05)	—
14gqr	2456951.88(0.05)	20.02(0.04)	—	—
14jhf	2457034.93(0.12)	19.14(0.15)	—	0.16(0.02)
14ym	2456715.42(1.10)	18.49(0.10)	0.38(0.05)	—
15acp	2457122.24(0.26)	20.33(0.08)	0.75(0.04)	0.64(0.03)
15dtg	2457372.83(0.06)	18.93(0.01)	0.09(0.01)	0.05(0.01)
16flq	2457644.56(0.30)	19.24(0.07)	0.16(0.01)	0.17(0.01)
16hgp	2457712.03(0.07)	19.36(0.04)	0.25(0.01)	0.16(0.03)

Table 3. Absolute magnitudes for 40 SNe in the r band (corrected for distance modulus and MW extinction), compared with the absolute magnitudes in the r band obtained when including the contribution from the host extinction with both methods, from the Na I D absorption and the $g - r$ method.

SN	$M_r^{\rm peak}$ no $\rm EBV_{host}$ (mag)	$M_r^{\rm peak}$ $\rm EBV_{host}$ from Na I D (mag)	$M_r^{\rm peak}$ $\rm EBV_{host}$ from $g - r$ (mag)
09dh	-18.88	-19.30	-19.25
09ut	-16.53	-16.53	-17.16
10bip	-17.52	-17.67	-17.52
10hfe	-16.75	-16.75	-16.75
10hie	-17.84	-17.89	-18.68
10lbo	-17.56	-17.56	-17.56
10osn	-16.90	-16.90	-17.05
10tqi	-17.15	-17.57	-17.62
10yow	-16.78	-17.23	-17.33
10zcn	-16.55	-16.85	-18.19
11bli	-17.42	-17.67	-18.69
11bov	-18.32	-18.44	-18.32
11jgj	-17.32	-17.90	-18.00
11klg	-17.26	-17.26	-17.99
11mnb	-18.29	-18.49	-18.50
11mwk	-18.39	-18.44	-18.39
11rka	-18.64	-18.85	-19.40
12cjy	-16.93	-16.93	-16.93
12dcp	-17.09	-17.09	-18.07
12dtf	-17.67	-17.78	-18.56
12fgw	-17.77	-17.77	-17.77
12gty	-19.73	-19.81	-19.84
12gzk	-18.65	-19.01	-19.19
12hvv	-17.37	-17.57	-19.18
12jxd	-16.04	-16.87	-17.14
12ktu	-16.38	-16.59	-17.25
13ab	-16.91	-17.02	-16.91
13aot	-16.90	-17.00	–
13cuv	-17.26	-17.30	-17.94
13dht	-16.87	-17.03	-17.38
13djf	-15.45	-15.53	-16.92
14bpy	-17.78	-17.78	-17.78
14fuz	-17.40	-17.52	-17.41
14gqr	-17.41	-17.41	-17.41
14jhf	-17.82	-18.62	–
14ym	-17.37	-17.76	-17.94
15acp	-18.77	-19.10	-19.62
15dtg	-18.00	-18.00	-18.28
16flq	-17.90	-18.51	-18.49
16hgp	-18.48	-18.48	-18.65

Table 4. Estimated explosions time (t_{explo}), the first detection ($t_{firstdet}$), estimated rise times in the r band ($t_{rise}(r)$) compared with the ones from the bolometric light curves ($t_{rise}(bolo)$) for the 44 SNe of our sample.

SN	t_{explo} (JD)	$t_{firstdet}$ (JD)	$t_{rise}(r)$ (days)	$t_{rise}(bolo)$ (days)
09dh	2454929.02	2454938.80	23.75	20.70
09ut	2454994.62	2455005.82	18.88	35.54
10bip	2455213.75	2455221.85	17.09	13.90
10hfe	2455324.83	2455331.87	15.57	12.44
10hie	2455323.06	2455335.96	12.38	15.80
10lbo	2455349.10	2455352.81	26.59	21.73
10osn	2455385.78	2455388.98	11.95	10.89
10tqi	2455426.96	2455429.98	16.00	13.66
10yow	2455467.01	2455467.61	13.41	12.36
10zcn	2455471.76	2455478.82	15.54	16.87
11bli	2455629.49	2455635.75	15.97	17.13
11bov	2455648.11	2455651.71	36.34	25.13
11hyg	2455735.62	2455738.92	14.82	14.96
11jgj	2455764.66	2455765.76	20.85	17.90
11klg	2455791.67	2455792.87	16.94	15.47
11lmn	2455794.29	2455801.74	16.97	21.19
11mnb	2455804.34	2455809.88	53.77	54.87
11mwk	2455811.23	2455820.83	16.55	14.31
11rka	2455895.61	2455896.01	32.54	33.67
12cjy	2455999.74	2456017.94	25.28	21.74
12dcp	2456027.93	2456033.96	19.62	28.69
12dtf	2456033.35	2456036.95	21.72	24.95
12fgw	2456077.64	2456077.74	14.90	13.62
12gty	2456086.82	2456086.82	72.38	52.64
12gzk	2456132.86	2456137.82	19.31	16.55
12hvv	2456148.97	2456151.87	16.51	28.63
12jxd	2456206.04	2456226.04	23.31	21.50
12ktu	2456227.59	2456231.89	17.24	19.50
13ab	2456308.78	2456327.88	23.89	19.34
13aot	2456394.05	2456395.85	22.09	–
13cuv	2456510.40	2456511.90	25.75	26.98
13dht	2456531.98	2456542.68	18.64	16.41
13djf	2456542.76	2456543.76	14.80	12.09
14bpy	2456821.20	2456823.70	13.78	11.19
14fuz	2456912.89	2456925.88	13.88	16.83
14gao	2456911.17	2456912.97	14.85	13.73
14gqr	2456944.25	2456944.34	7.18	6.06
14jhf	2457008.50	2457011.90	25.08	–
14ym	2456692.23	2456711.03	22.48	18.23
15acp	2457105.67	2457107.97	14.56	12.74
15cpq	2457268.87	2457270.87	15.69	12.95
15dtg	2457333.45	2457333.93	37.41	19.88
16flq	2457617.46	2457627.96	25.57	19.34
16hgp	2457678.69	2457681.79	30.90	21.76

Table 5. Estimated Fe II λ5169 velocities at peak for 44 SNe of the sample

SN	v_{max} (km s^{-1})
09dh	8125.6
09ut	8125.6
10bip	13706.70
10hfe	9497.55
10hie	10108.39
10lbo	9140.21
10osn	4589.67
10tqi	9315.55
10yow	9464.53
10zcn	8819.06
11bli	4847.10
11bov	5815.18
11hyg	7832.18
11klg	8172.07
11jgj	8125.6
11lmn	2437.49
11mnb	5005.96
11mwk	8573.56
11rka	5739.87
12cjy	8125.6
12dcp	6493.21
12dtf	8894.58
12fgw	8125.6
12gty	3492.84
12gzk	16984.08
12hvv	8076.82
12jxd	7831.30
12ktu	8319.47
13ab	11149.58
13aot	7728.21
13cuv	5389.32
13dht	7065.56
14djf	8125.6
14bpy	11148.79
14fuz	9754.77
14gao	10171.24
14gqr	10472.35
14jhf	7989.49
14ym	7436.66
15acp	6570.15
15cpq	9960.42
15dtg	8261.14
16flq	6281.47
16hgp	6235.76

Table 6. Estimated explosion parameters for the 42 SNe.

SN	M_{ej} ($M_\odot$)	E_K (10^{51} erg)	$M_{^{56}\mathrm{Ni}}$ ($M_\odot$)
09dh	1.99 (0.79)	0.80 (0.16)	0.46 (0.05)
09ut	8.73 (3.47)	3.50 (0.70)	0.07 (0.01)
10bip	3.99 (1.59)	4.47 (0.89)	0.13 (0.01)
10hfe	1.23 (0.49)	0.66 (0.13)	0.09 (0.01)
10hie	3.19 (1.27)	1.95 (0.39)	0.12 (0.01)
10lbo	7.53 (3.00)	3.75 (0.75)	0.18 (0.02)
10osn	0.58 (0.23)	0.07 (0.01)	0.05 (0.01)
10tqi	2.49 (0.99)	1.29 (0.26)	0.09 (0.01)
10yow	2.45 (0.98)	1.31 (0.26)	0.06 (0.01)
10zcn	2.70 (1.07)	1.25 (0.25)	0.06 (0.01)
11bli	2.21 (0.88)	0.31 (0.06)	0.17 (0.02)
11bov	7.11 (2.83)	1.43 (0.29)	0.47 (0.05)
11hyg	2.10 (0.83)	0.77 (0.15)	0.11 (0.01)
11jgj	4.63 (1.84)	1.86 (0.37)	0.15 (0.02)
11klg	2.54 (1.01)	1.01 (0.20)	0.08 (0.01)
11lmn	1.47 (0.58)	0.24 (0.05)	0.15 (0.02)
11mnb	31.29 (12.45)	4.68 (0.94)	0.74 (0.08)
11mwk	2.77 (1.10)	1.22 (0.24)	0.28 (0.03)
11rka	13.29 (5.29)	2.61 (0.52)	0.67 (0.07)
12cjy	0.43 (0.17)	0.17 (0.03)	0.06 (0.01)
12dcp	4.16 (1.65)	1.05 (0.21)	0.10 (0.01)
12dtf	7.87 (3.13)	3.74 (0.75)	0.19 (0.02)
12fgw	0.50 (0.20)	0.20 (0.04)	0.27 (0.03)
12gty	21.42 (8.52)	1.56 (0.31)	2.98 (0.30)
12gzk	6.31 (2.51)	10.85 (2.17)	0.41 (0.04)
12hvv	10.30 (4.10)	4.01 (0.80)	0.22 (0.02)
12jxd	0.62 (0.25)	0.23 (0.05)	0.03 (0.01)
12ktu	4.02 (1.60)	1.66 (0.33)	0.04 (0.01)
13ab	0.24 (0.10)	0.18 (0.04)	0.05 (0.01)
13cuv	6.24 (2.48)	1.08 (0.22)	0.13 (0.01)
13dht	3.43 (1.36)	1.02 (0.20)	0.07 (0.01)
13djf	3.79 (1.51)	1.52 (0.30)	0.02 (0.01)
14bpy	1.62 (0.65)	1.20 (0.24)	0.13 (0.01)
14fuz	3.76 (1.49)	2.13 (0.43)	0.10 (0.01)
14gao	1.42 (0.56)	0.87 (0.17)	0.06 (0.01)
14gqr	0.12 (0.05)	0.08 (0.02)	0.06 (0.01)
14ym	0.55 (0.22)	0.18 (0.04)	0.09 (0.01)
15acp	1.61 (0.64)	0.42 (0.08)	0.47 (0.05)
15cpq	1.43 (0.57)	0.85 (0.17)	0.28 (0.03)
15dtg	6.10 (2.42)	2.48 (0.50)	0.25 (0.02)
16flq	7.39 (2.94)	1.74 (0.35)	0.36 (0.04)
16hgp	5.64 (2.24)	1.31 (0.26)	0.41 (0.04)

Table 7. Comparison of the average estimates of the explosions parameters with estimates from the literature.

	$M_{^{56}\mathrm{Ni}}$ ($M_\odot$)	M_{ej} (10^{51} erg)	E_K ($M_\odot$)
Drout+11	0.24 (0.15)	$1.7^{+1.4}_{-0.9}$	$1.0^{+0.9}_{-0.5}$
Taddia+15	0.33 (0.11)	5.7 (3.6)	1.7 (0.4)
Lyman+16	0.22 (0.16)	3.0 (2.8)	1.9 (1.3)
Prentice+16	$0.16^{+0.03}_{-0.10}$	...	...
Taddia+18	0.13 (0.04)	2.1 (1.0)	1.2 (0.7)
Prentice+19	0.11 (0.09)	3.0 (0.7)	...
This work[a]	0.19 (0.05)	4.39 (0.31)	1.71 (0.16)
This work[b]	0.15 (0.06)	3.54 (0.30)	1.50 (0.15)
This work[c]	0.15 (0.05)	3.94 (1.07)	1.54 (0.19)

[a] Avarage values for the overall sample of 41 SNe

[b] Average values when the 6 SNe with broad light curve are excluded

[c] Average values when the 6 SNe with broad light curve and the 1 fast SN are excluded

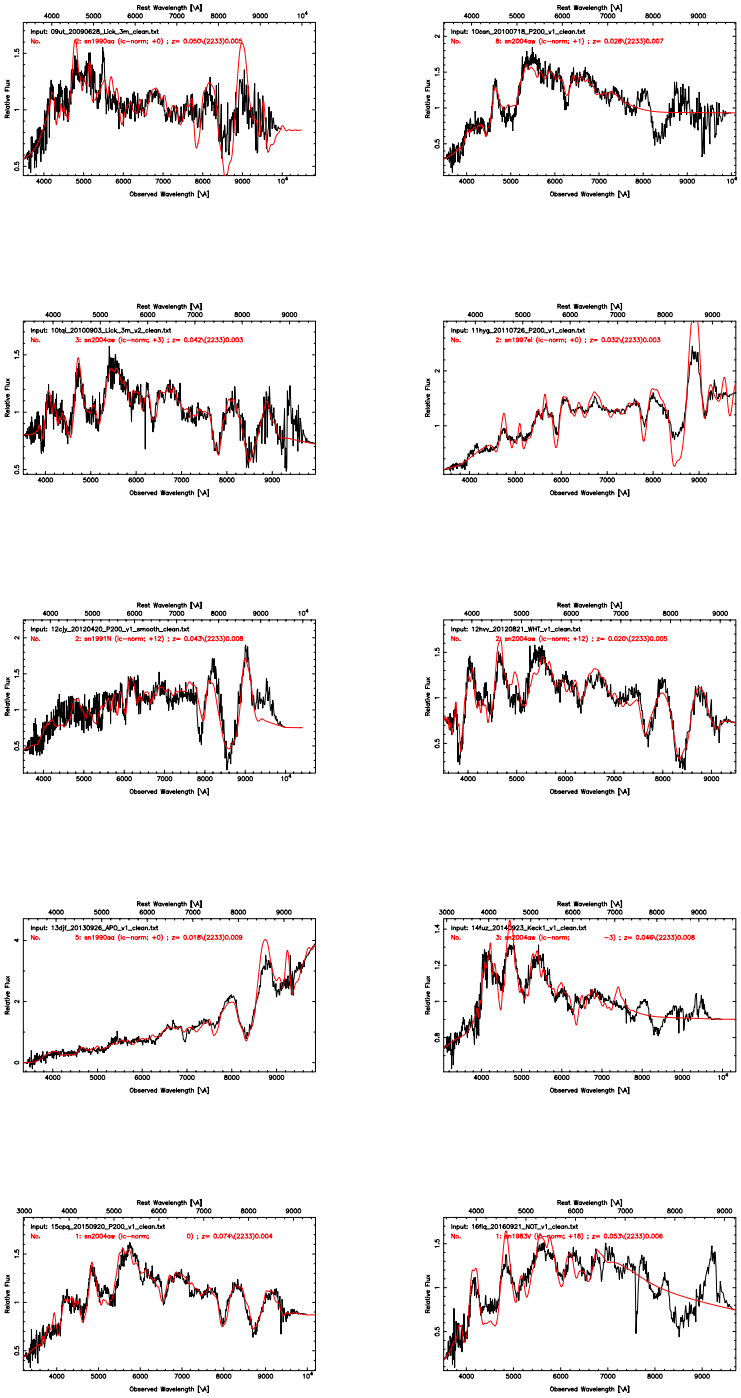

Fig. 1. Examples of 10 SNe from the sample and their classification through the SNID package.

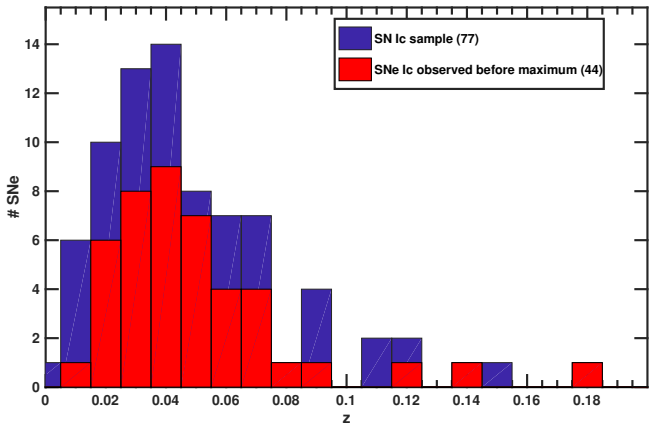

Fig. 2. Redshift distribution of all (i)PTF SNe Ic (blue) and of the 44 SNe Ic discovered before peak (red). The latter constitute the sample analysed in this work.

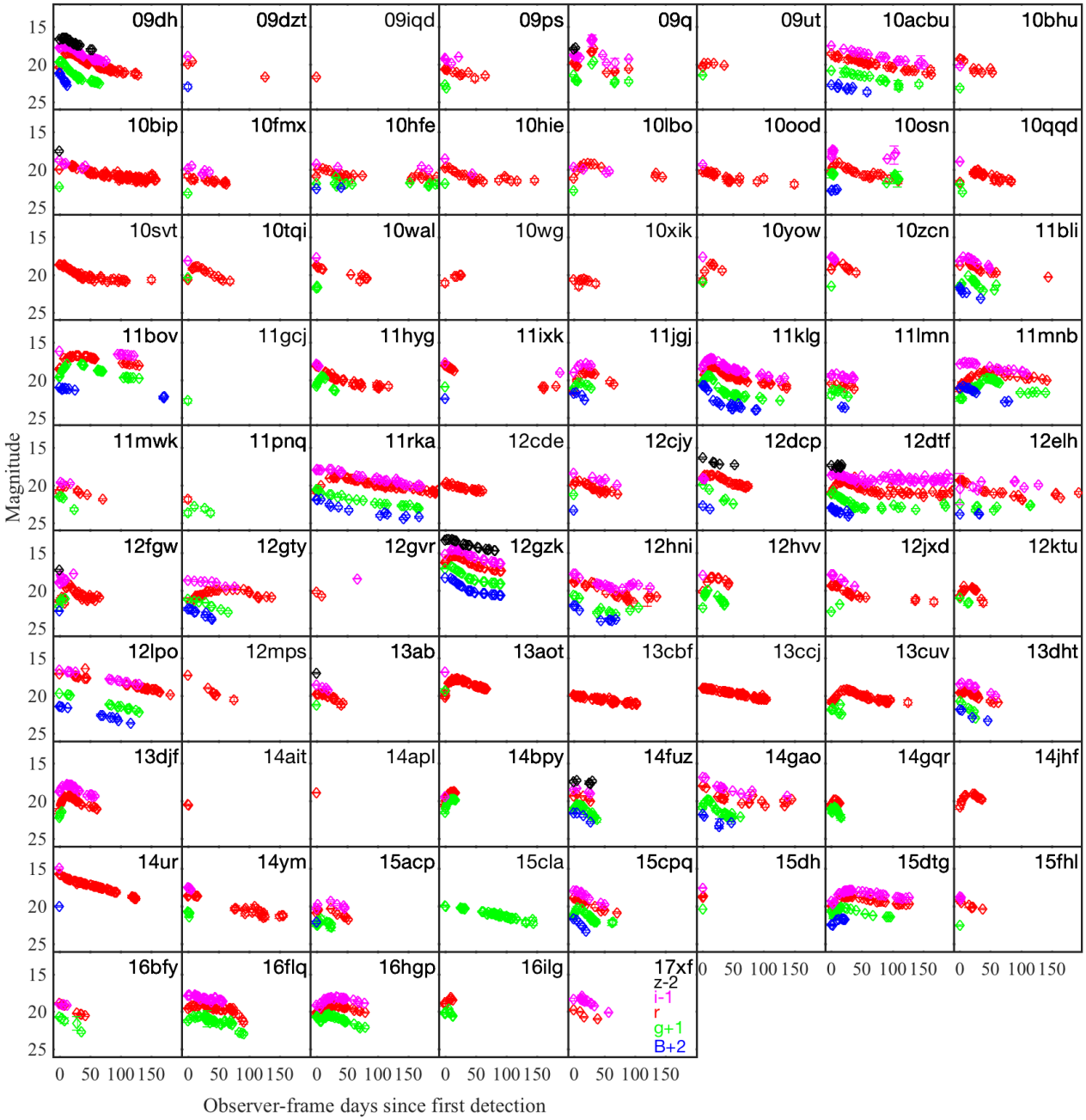

Fig. 3. Light curves for all the 60 SNe Ic and the 17 SNe Ibc in (i)PTF. We plot the apparent magnitude as a function of time since first detection, in the observer frame. Shifts have been applied for clarity as indicated in the legend in the bottom row.

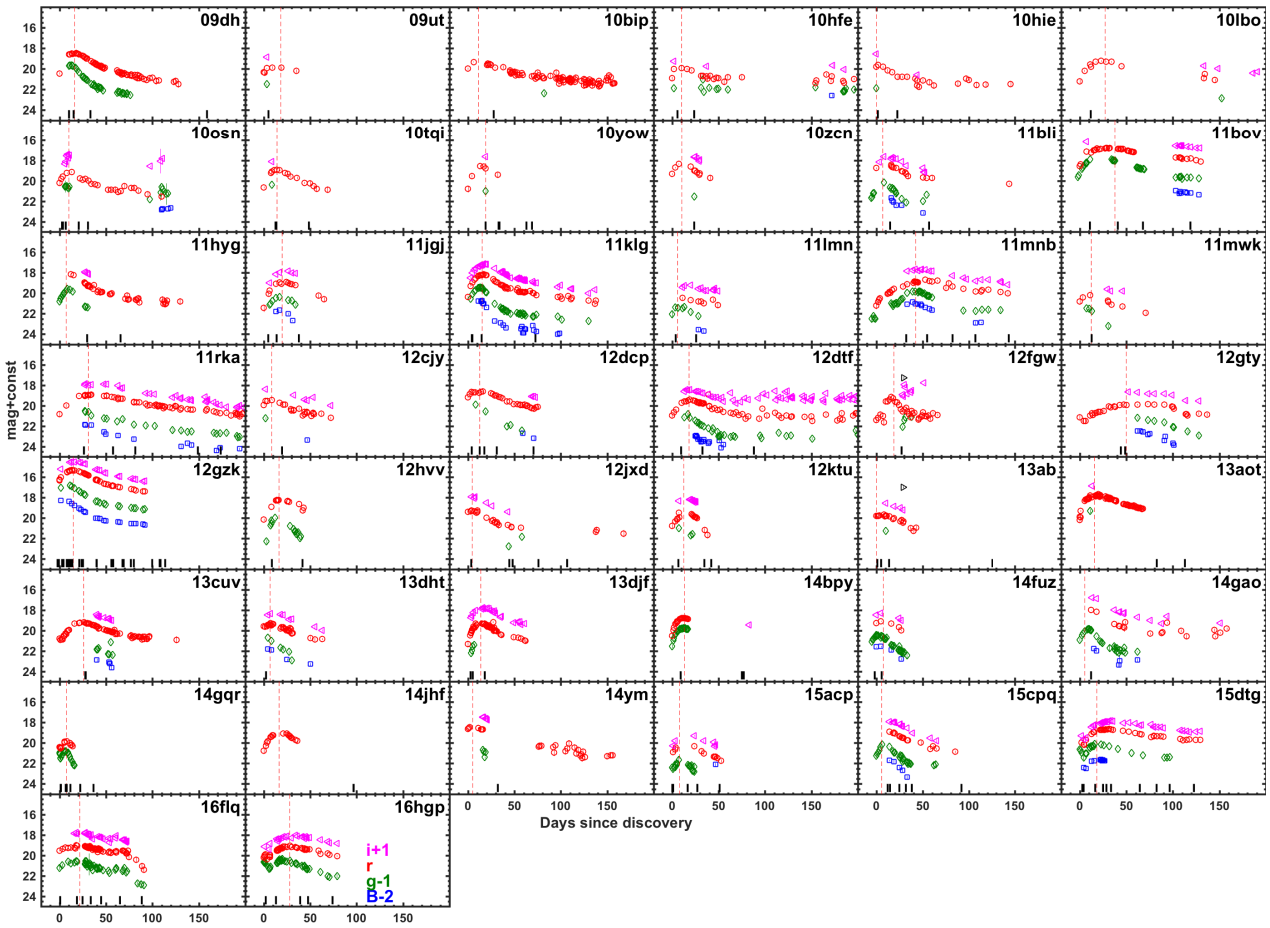

Fig. 4. Light curves in B, g, r, i of the 44 SNe Ic for which we have pre-maximum observations. We plot the apparent magnitude as a function of days since discovery. Shifts have been applied for clarity, as indicated in the legend in the bottom row. The peak epoch is shown as a dashed red line. The black dashed lines at the bottom represent epochs of spectral observations.

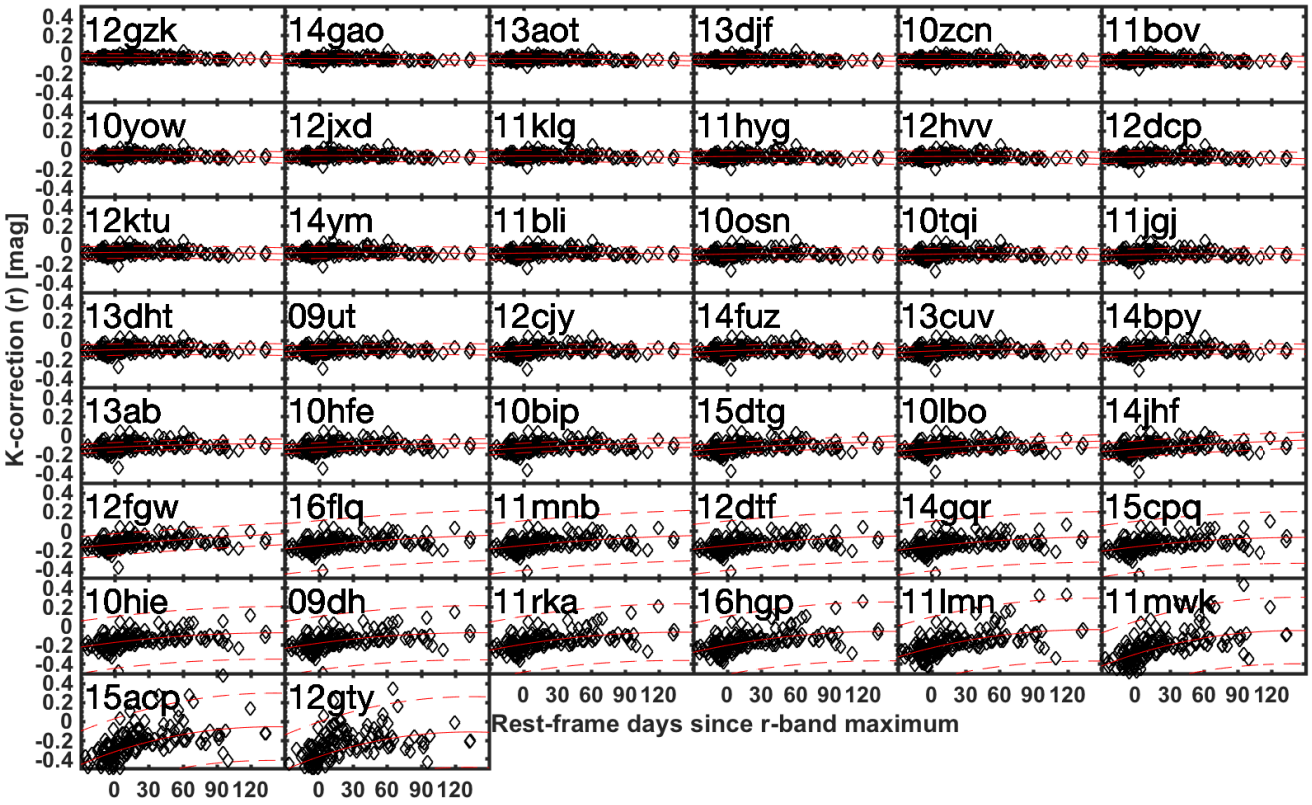

Fig. 5. K-corrections in the *r* band for our SN sample. The solid red line represents the second order polynomial fit, whereas the red dashed lines show the 1 σ uncertainties. The SNe have been ordered according to increasing redshift.

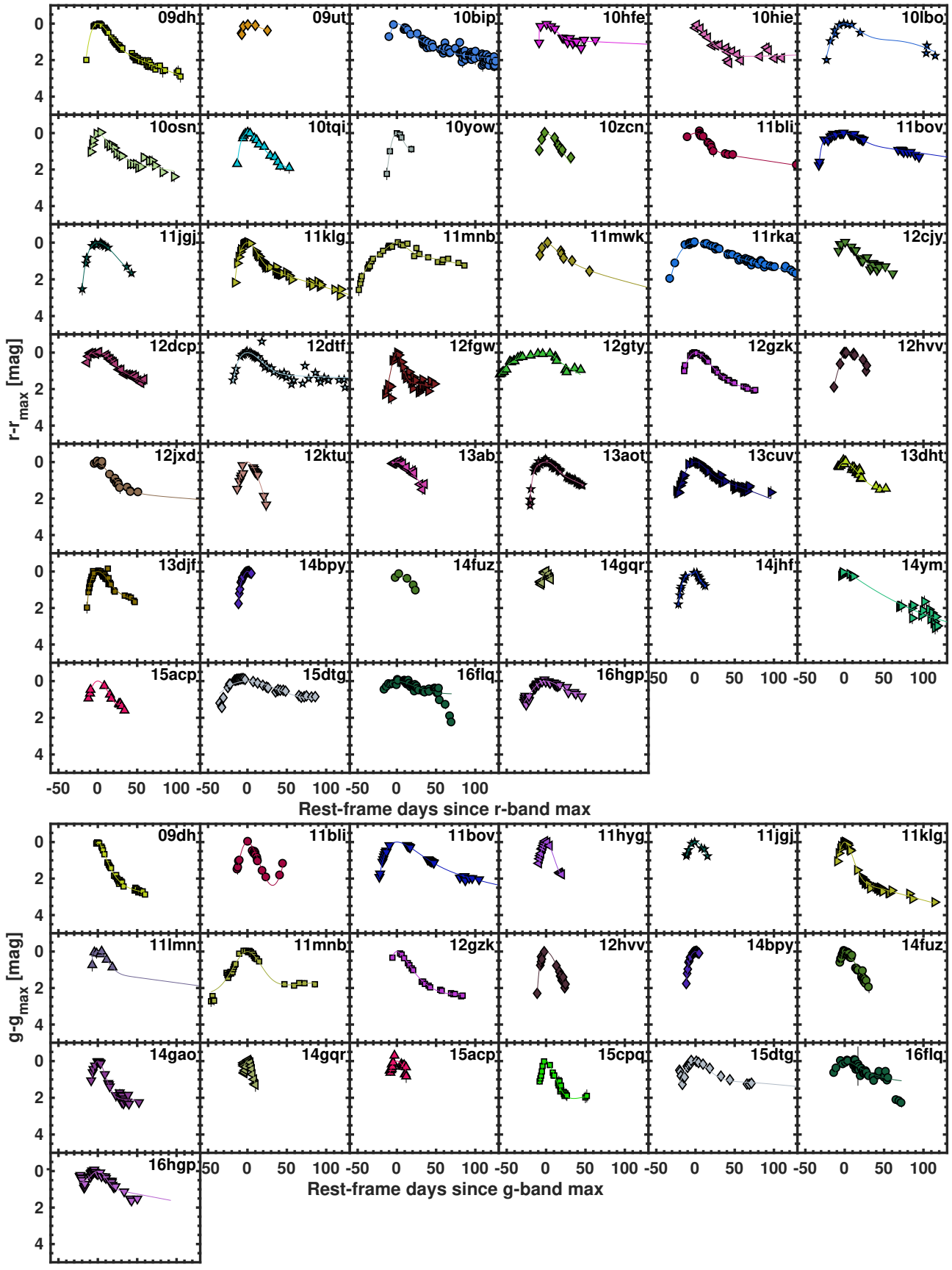

Fig. 6. `Upper panel:` Individual 40 SNe and their Contardo fits in the *r* band. `Lower panel:` Individual 19 SNe and their Contardo fits in the *g* band.

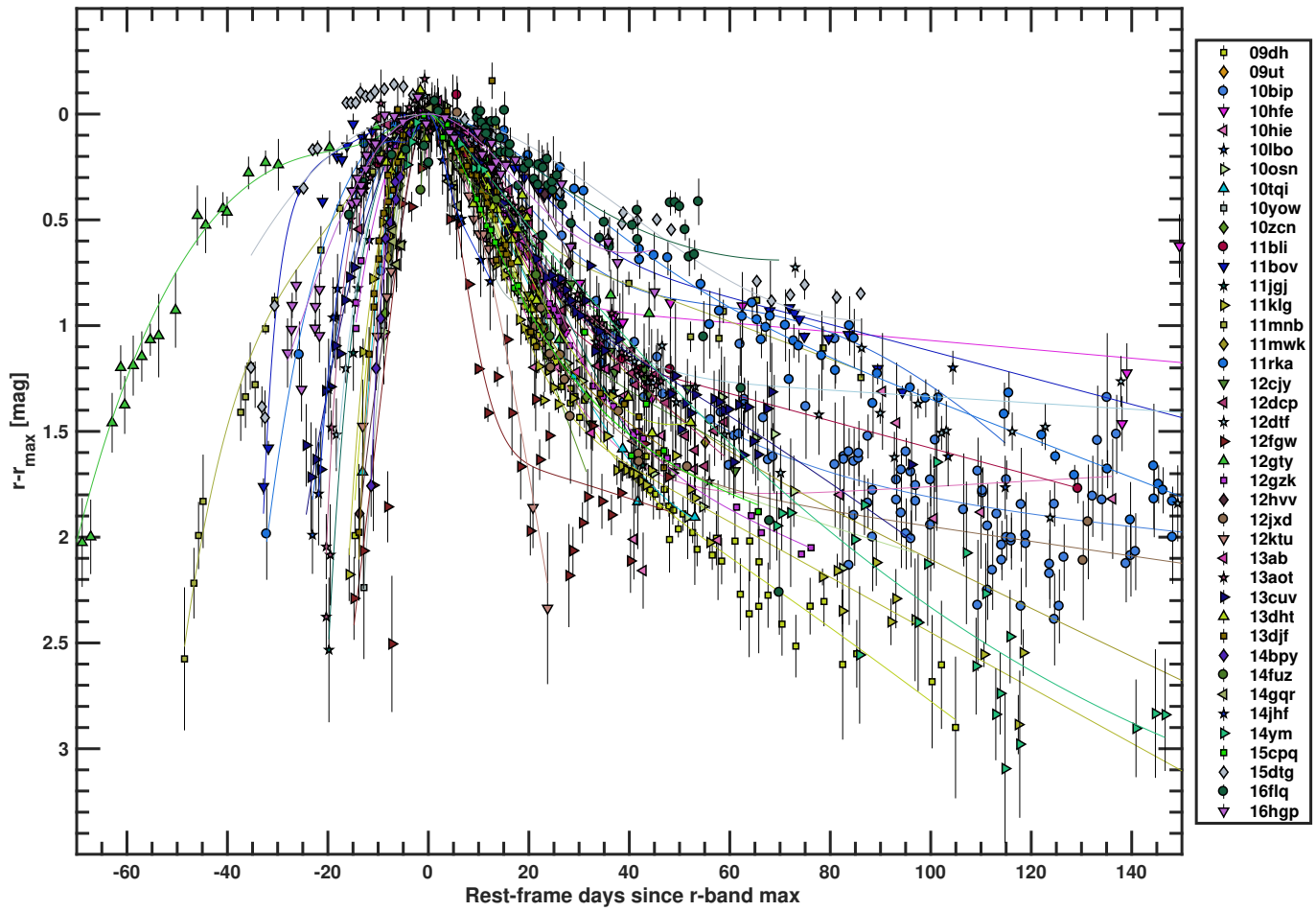

Fig. 7. These are the *r*/band light curves for our 40 SNe Ic plotted together. The best Contardo fits are included as full lines. In this and following plots the individual SNe are represented with symbols and colors as provided in the legend to the right. The light curves are normalised at peak in order to illustrate their diversity.

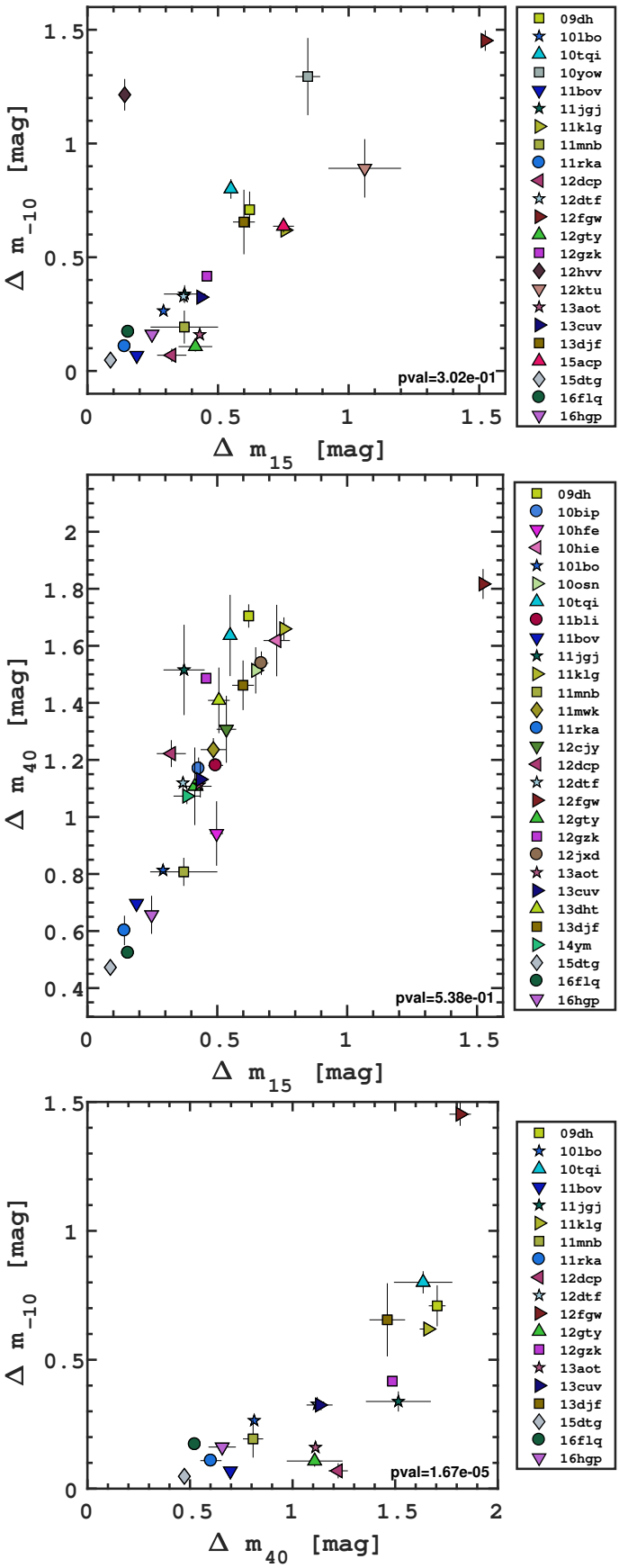

Fig. 8. Correlations between rise and decay in the r band. `Upper panel:` The plot shows Δm_{15} against Δm_{-10}. `Mid panel:` Δm_{15} versus Δm_{40}. `Lower panel:` The plot shows Δm_{40} against Δm_{-10}.Plots show a correlation among parameters and their p−values are also reported.

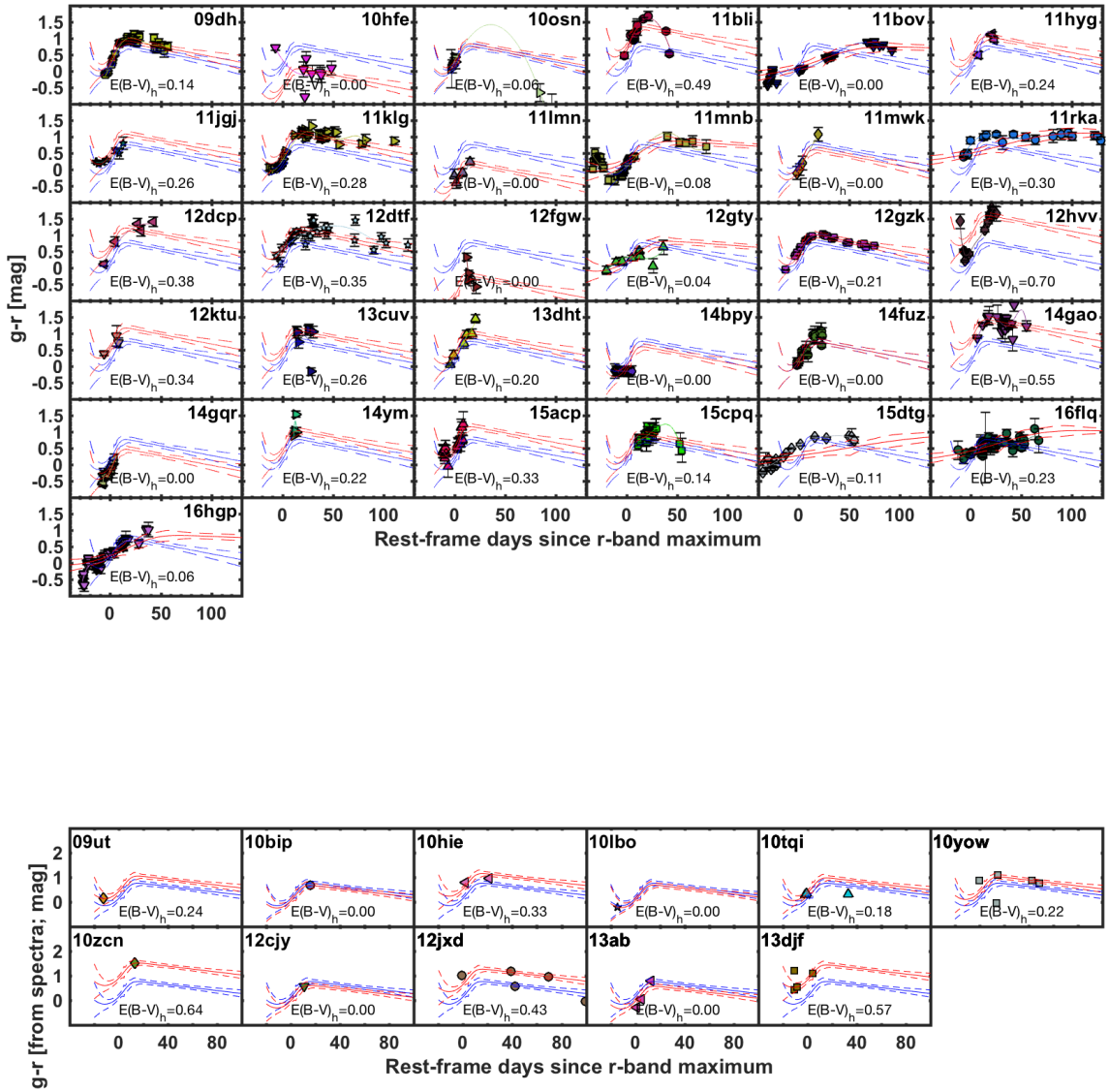

Fig. 9. `Upper panel:` Individual (MW corrected) $g - r$ colour evolution for 31 SNe from photometry with the polynomial fits represented as solid lines. The red lines represent the fit of the data with the $g - r$ template. The blue line is the template for a Type Ic with no extinction from Stritzinger et al. (2017), and each panel shows the reddening in E(B−V) required to shift the colour curve to the data. This represents the estimated host extinction measured in magnitudes. `Bottom panel:` Same as above for the 11 SNe where the colours are calculated from spectroscopy.

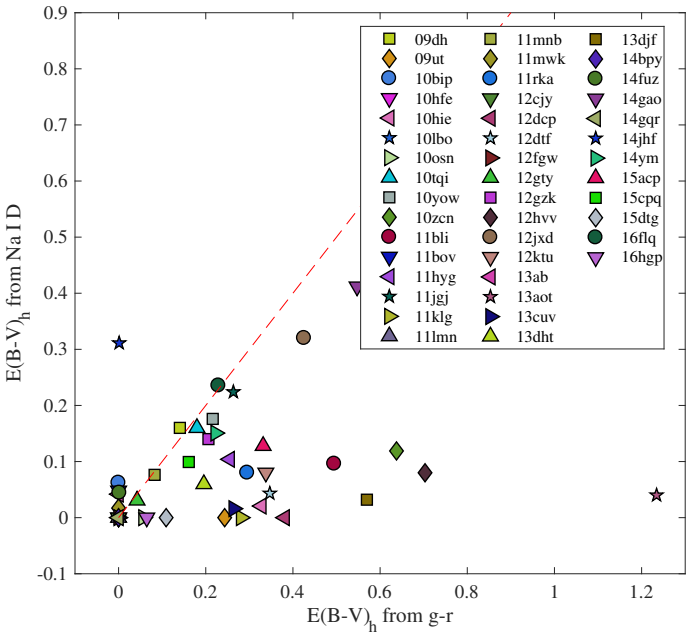

Fig. 10. A comparison between the extinction estimated from the Na ID absorption versus that estimated from the $g - r$ colour evolution. The red line represents a one-to-one relation, but clearly the Na ID gives consistently lower estimates. Units are in magnitudes.

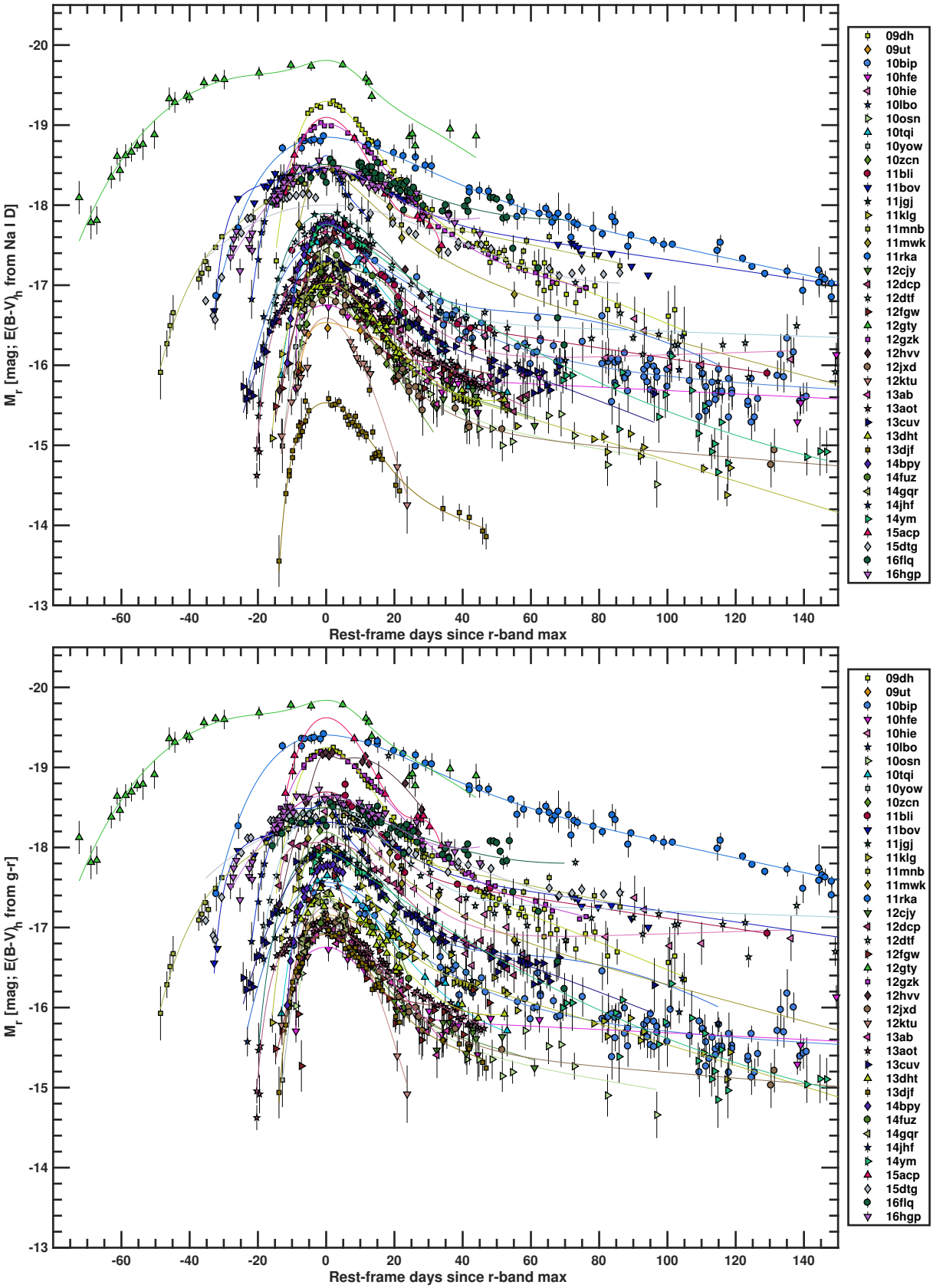

Fig. 11. `Upper panel:` Absolute magnitude in r band of the 40 SNe of the sample when extinction is estimated from the Na ID absorption. `Bottom panel:` Absolute magnitude in r band of the 40 SNe of the sample when extinction is estimated from $g - r$ colour evolution. For SNe iPTF13aot and iPTF14jhf we assumed the extinction from the Na ID in both cases, since there is no estimate from $g - r$.

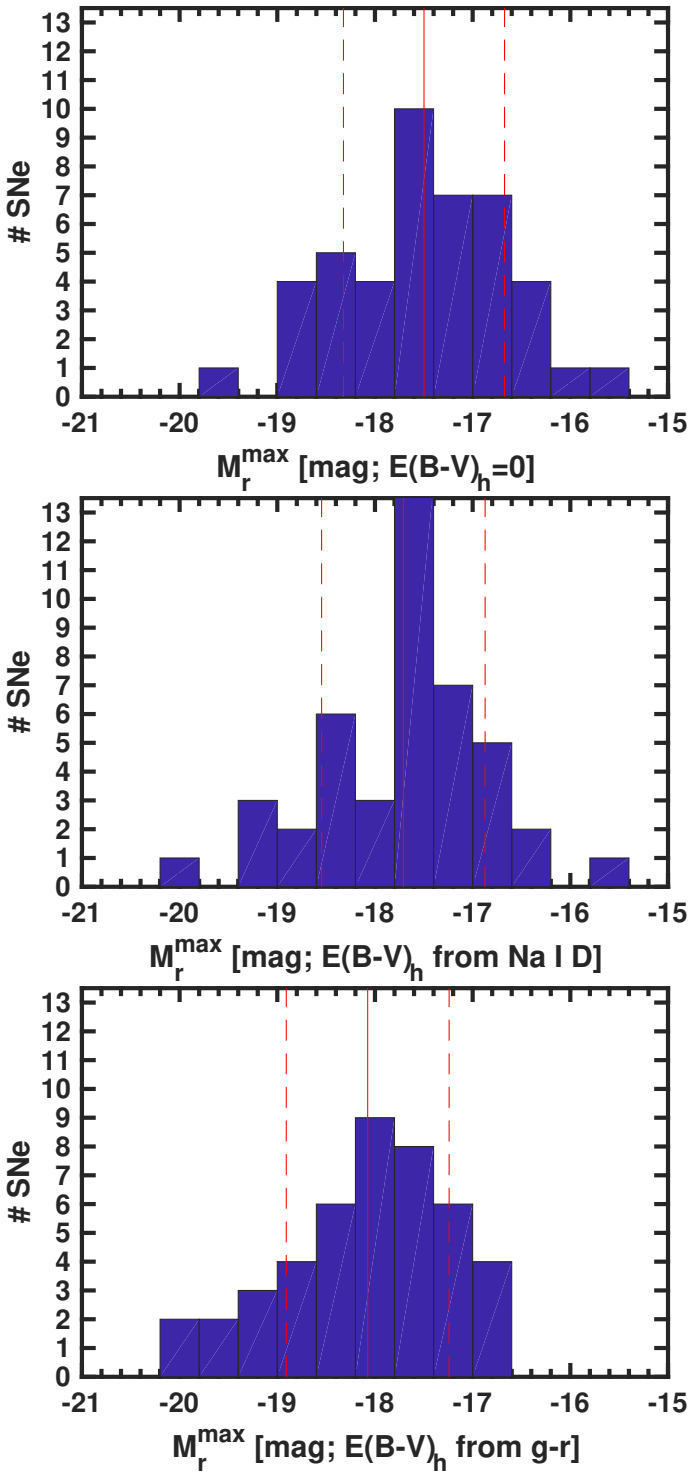

Fig. 12. Histogram representation of the absolute magnitudes at peak in the *r*-band distribution of the sample. `Upper panel` Distribution obtained correcting for the distance and the MW extinction. `Middle panel` Distribution obtained including also the extinction from the host galaxy, estimated through the Na ID absorption. `Bottom panel` Distribution obtained including instead the host extinction from the colours.

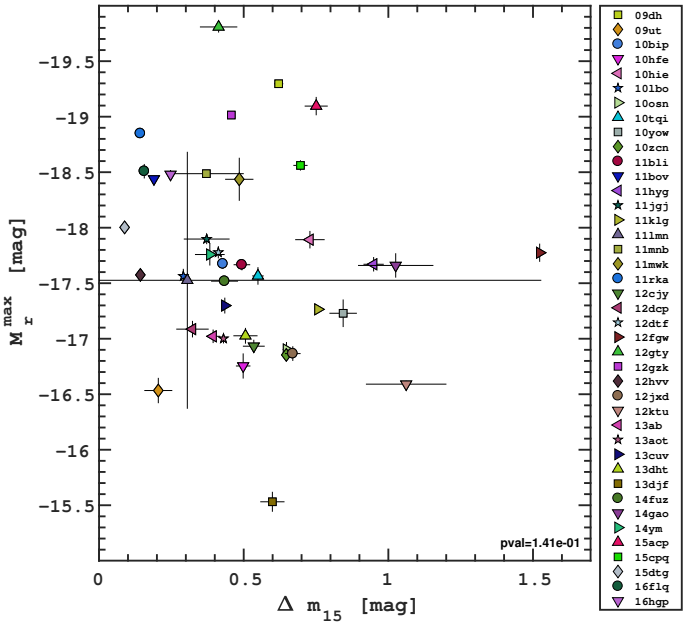

Fig. 13. Philip-like relation: peak absolute *r*-band magnitude vs Δm_{15}. The plot show no correlation.

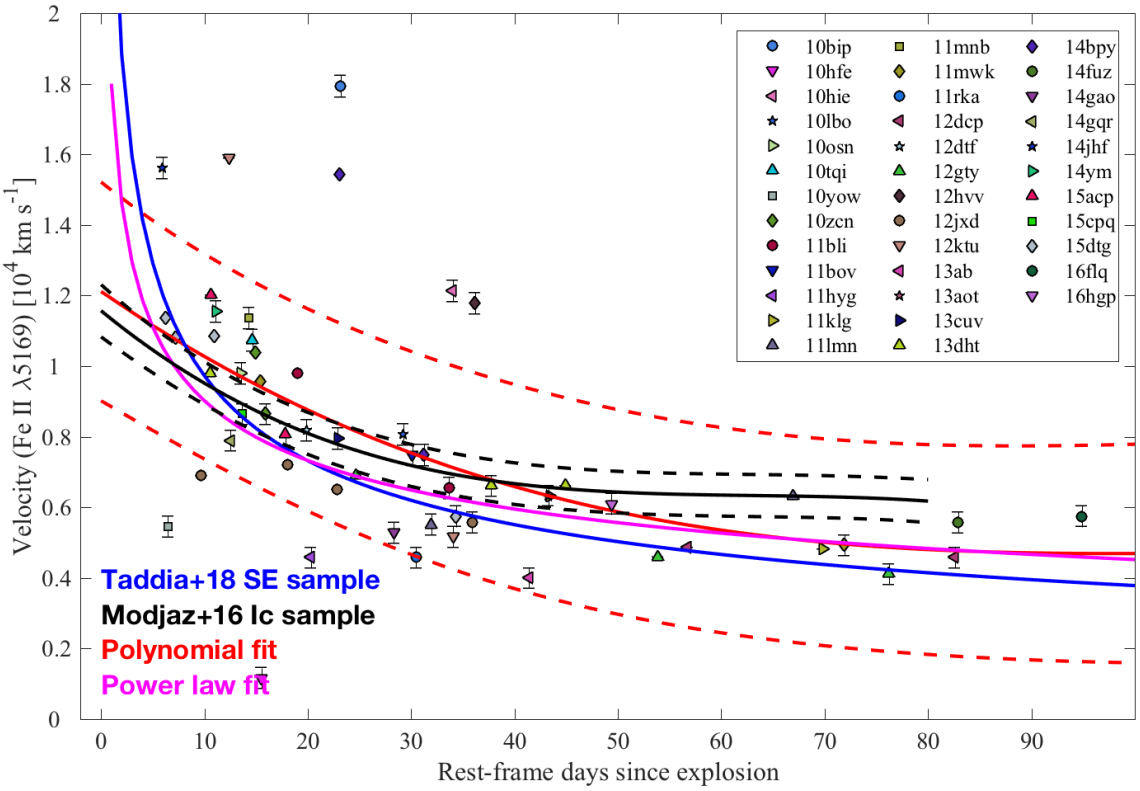

Fig. 14. Fe II λ5169 velocity evolution for 37 SNe Ic from the sample (see Sect. 6.1 for the selection criteria). The magenta solid line represents the power law that fits the evolution with time. The blue solid line represents the trend found by Taddia et al. (2018b) and is similar to the one found in this work. The black lines represent the polynomial fit found by Modjaz et al. (2016). As a comparison, we fitted the data also with a polynomial fit, here shown in red.

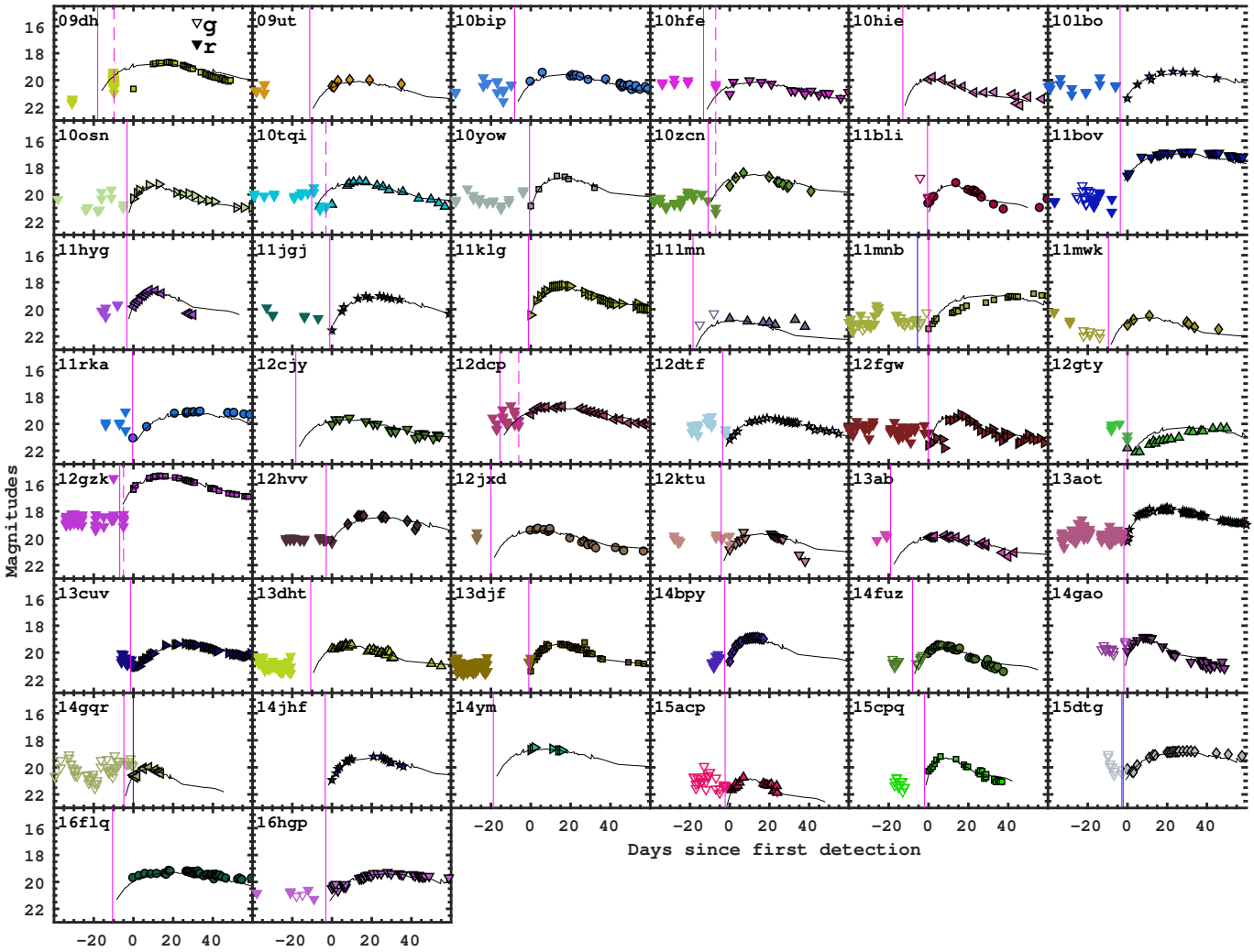

Fig. 15. The plot shows the fit of the light curve of iPTF13djf to the other SNe of the sample to estimate the explosion epoch. The open symbols represents the pre-explosion limits. Solid magenta lines represent the explosion epochs estimated from the fit. Dashed magenta lines represent the last non-detection assumed as explosion epoch. Blue solid lines represent explosion epochs available from literature.

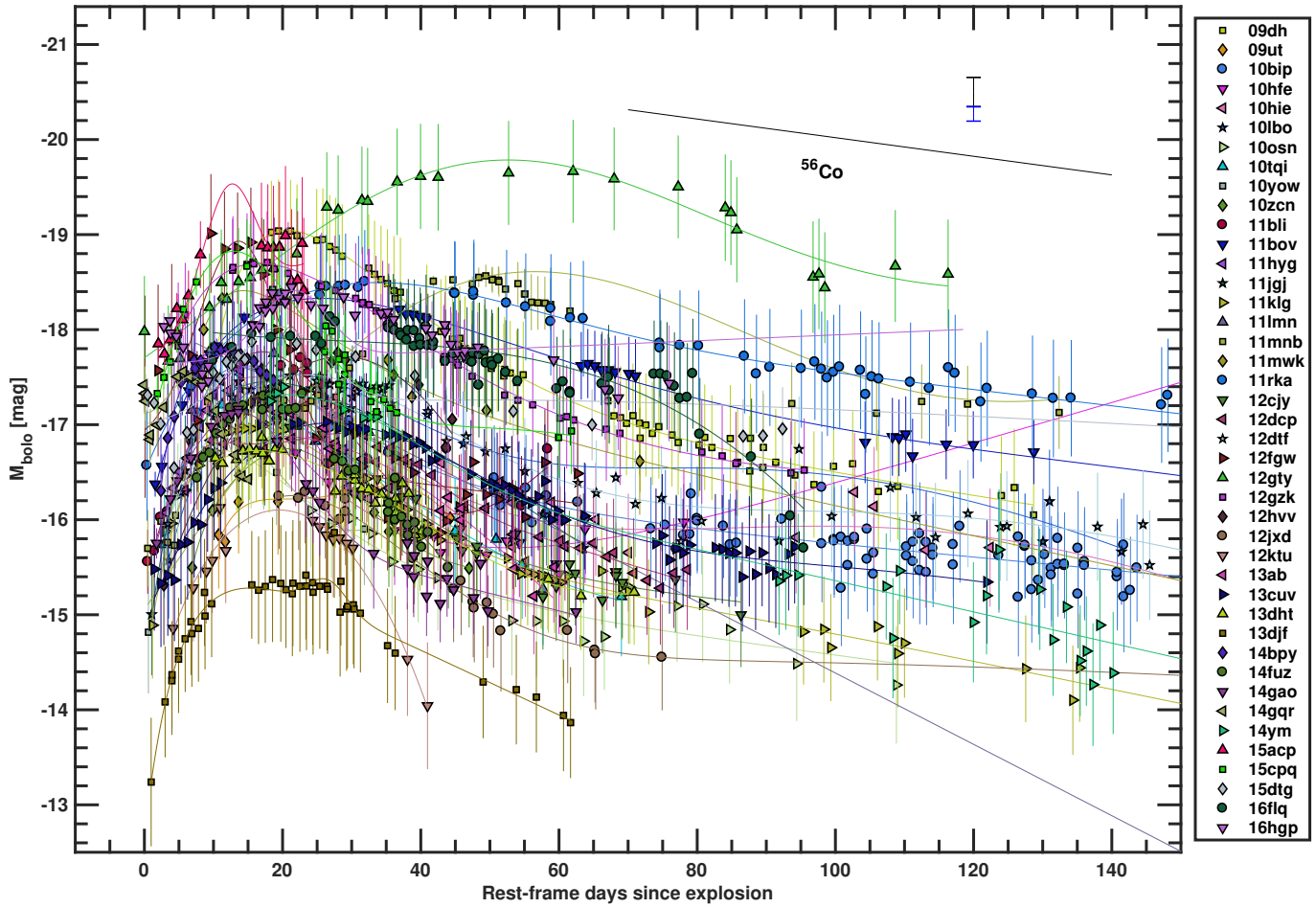

Fig. 16. Bolometric light curves of 42 Type Ic SNe . The solid lines represent the Contardo fits performed on every individual light curve. The slope of the radioactive cobalt decay, 0.098 mag per day is illustrated in the upper right corner. There we also include a representative error bar that includes the uncertainty in distance, and extinction, respectively, which are not included in the errors on the data points.

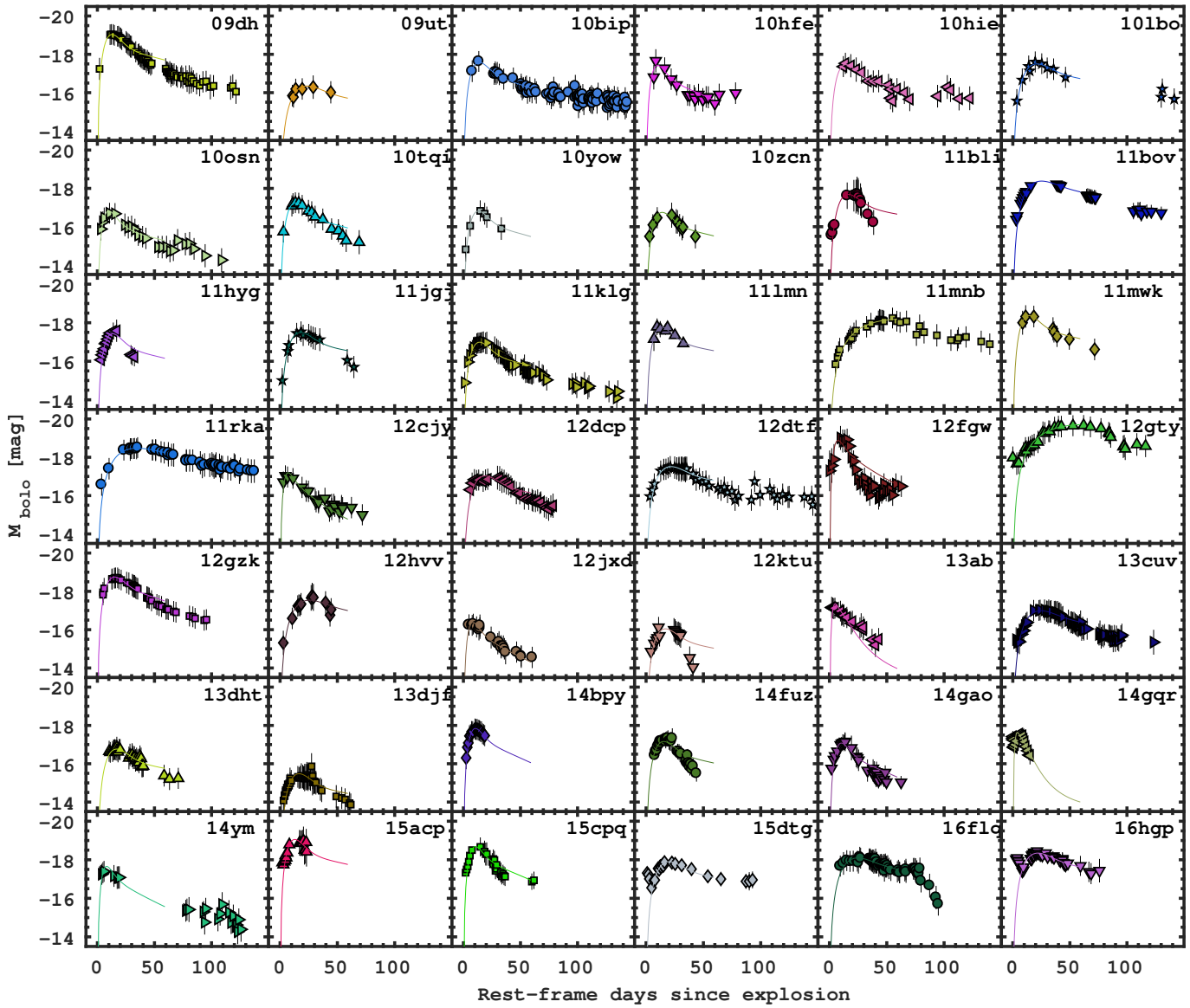

Fig. 17. The plot shows the bolometric light curve computed and fitted with Arnett model for the 42 SNe of the sample.

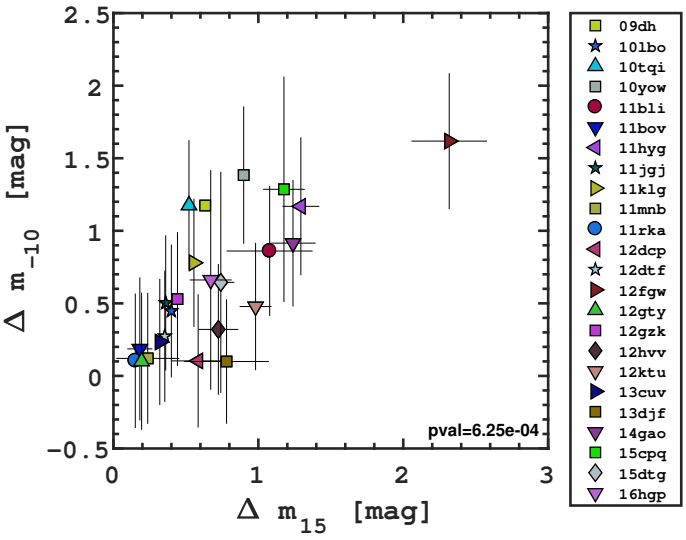

Fig. 18. Bolometric light curve shape: Δm_{15} vs Δm_{-10}. The plot does show a correlation, as also found in the r−band..

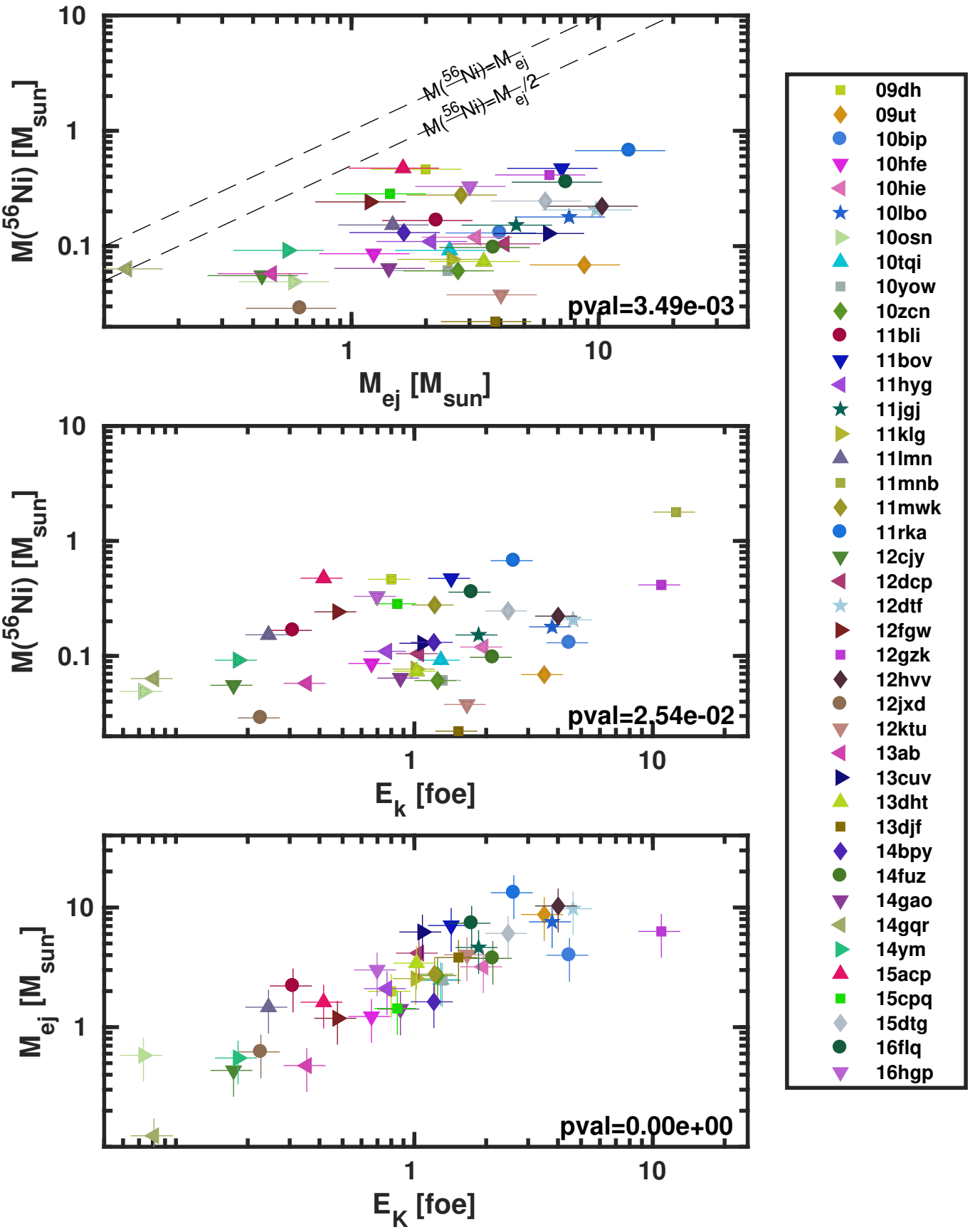

Fig. 19. Explosions parameters for 41 SNe Ic plotted against each other. We see clear correlations between the parameters, as quantified by the p-values in the panels.

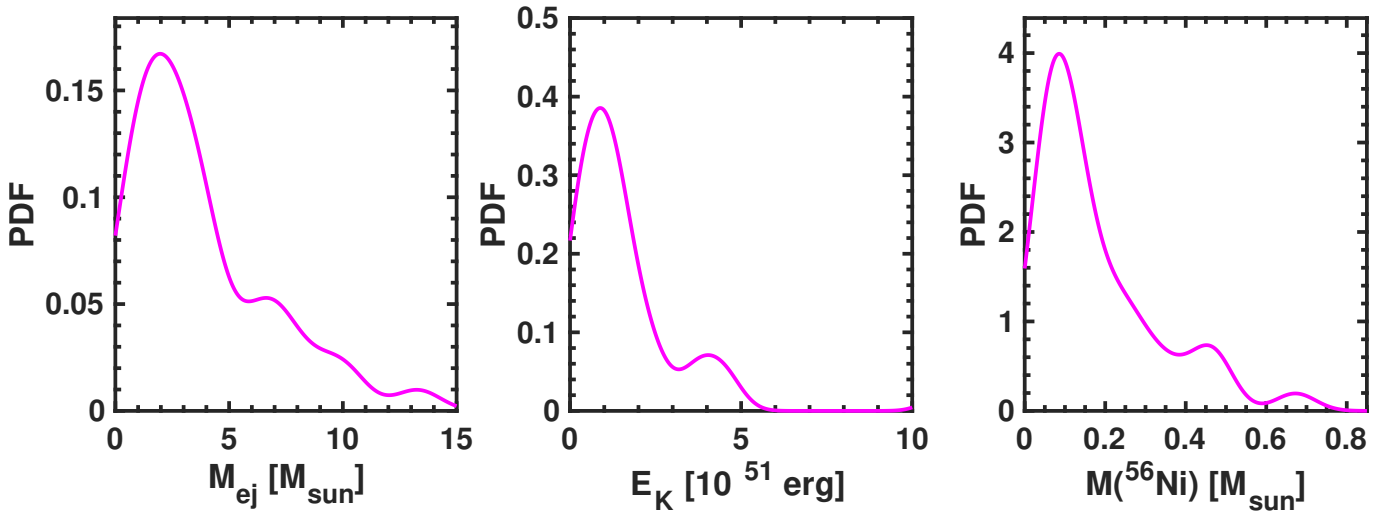

Fig. 20. Probability density functions for explosion parameters for our sample of SNe Ic

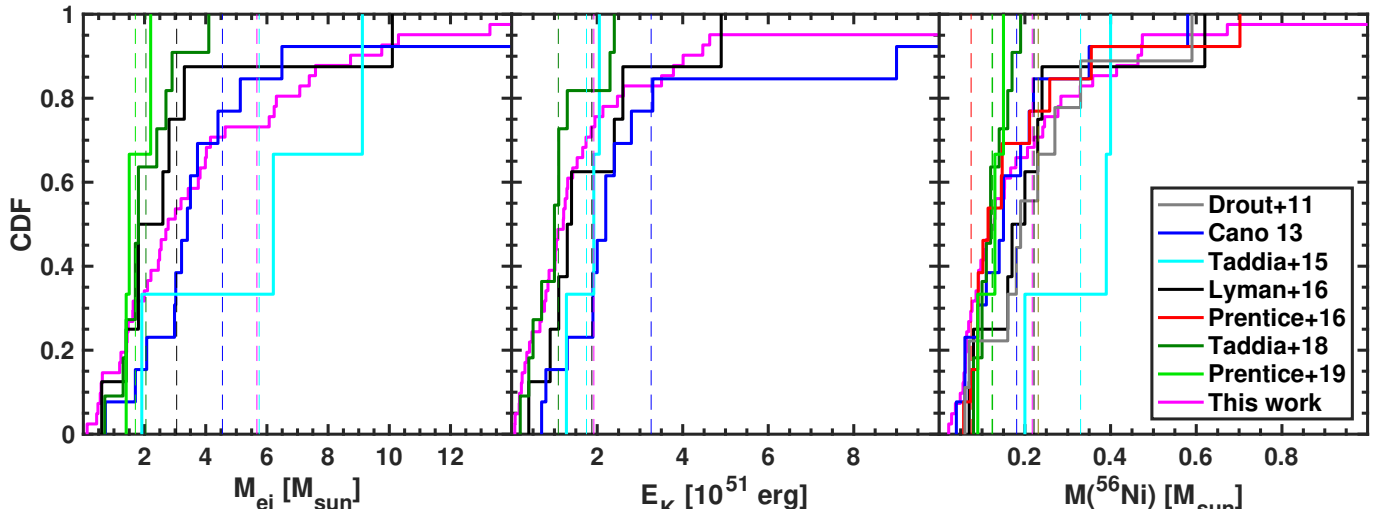

Fig. 21. Cumulative distribution functions for the explosion parameters compared to those of other samples in the literature.